本科生毕业论文

题目： **开放量子拉比模型耗散性相变的实验探究**

Experimental Study on Dissipative Phase

Transition in the Open Quantum Rabi Model

姓　　名：　　　　周子楠

学　　号：　　　1600018413

院　　系：　　　物理学院

专　　业：　　　物理学

导　　师：　　　金奇奂

二〇二一年六月

版权声明

任何收存和保管本论文各种版本的单位和个人，未经本论文作者同意，不得将本论文转借他人，亦不得随意复制、抄录、拍照或以任何方式传播。否则一旦引起有碍作者著作权之问题，将可能承担法律责任。

摘要

量子光学从量子化的角度出发研究物质和电磁场的相互作用。量子拉比模型（quantum Rabi model, QRM）描述的是一个二能级系统和单个玻色模式的相互作用，是最简单的量子光学系统之一。其哈密顿量为

$$H_{\mathrm{QRM}} = \omega_0 a^\dagger a + \frac{\Omega}{2}\sigma_z - \lambda\sigma_x\left(a + a^\dagger\right).$$

其中 λ 反映了二能级和玻色模式的耦合强度。在弱耦合的条件 $|\omega_0 - \Omega| \ll |\omega_0 + \Omega|$ 下，通过旋转波近似略去高频旋转项，就得到 Jaynes-Cummings 模型（JCM）

$$H_{\mathrm{JCM}} = \omega_0 a^\dagger a + \frac{\Omega}{2}\sigma_z - \lambda\left(\sigma_+ a + \sigma_- a^\dagger\right).$$

该模型简洁深刻地体现了光和物质相互作用的本质，在 20 世纪后半叶以来已经得到了充分的研究，取得了不菲的成果。近年来，实验技术的进步使得在强耦合条件下模拟 QRM 也成为了可能。并且随着 Braak 在 2011 年首先证明了 QRM 的可积性，其解析解得到了更多研究，产生了很多理论结果，这些理论结果又促使了我们对其进行实验上的验证。根据 λ/ω_0 的取值不同，通常将 QRM 的耦合情况分为三类：$\lambda/\omega_0 \ll 1$ 的 Jaynes-Cummings 区，$0.1 \lesssim \lambda/\omega_0 \lesssim 1$ 的超强耦合（ultrastrong coupling, USC）区，和 $\lambda/\omega_0 \gtrsim 1$ 的深强耦合（deep strong coupling, DSC）区。2018 年，我组的吕定顺前辈业已成功根据 I. Lizuain 的方案，使用离子阱系统模拟了 QRM，并观察到 DSC 区旋转波近似不成立的现象。我们感兴趣的从正常态到超辐射（superradiant）态的相变就发生在 DSC 区。

量子相变（quantum phase transition）近年来得到越来越多的关注。从数学的结构上看，它和经典的热相变是相似的，量子相变的临界点指的是基态能量随着某个参数发生改变时，不解析的点。从物理上看，热相变是热涨落同系统自身相互作用的竞争，而量子相变发生在零温处，不存在热涨落，与相互作用竞争的是由 Heisenberg 不确定关系给出的量子涨落。

最早的量子相变研究使用的是晶格系统，容易理解，只有在晶格的尺度 $L \to \infty$ 时，相变才会发生。而 QRM 中的量子相变较为特殊，它仅仅由单个量子比特和单个玻色模式组成，理论研究表明在这一系统中，频率比 Ω/ω_0 起到了类似 L 的作用。

我们的实验方案基于 Ricardo Puebla，黄明重（Myung-Joong Hwang），Martin B Plenio

等近年来关于 QRM 相变的一系列研究结果。在论文中，我们对部分理论结果进行了数值计算确认。

在 $\Omega/\omega_0 \to \infty$ 的极限条件下，QRM 的本征值和本征态可以求出解析解，据此不仅可以找到临界点，还可以求出我们关心的观测量 A 的临界指数 κ_A。定义无量纲的耦合系数 $g \equiv 2\lambda/\sqrt{\omega_0\Omega}$，结论如下：

$$g_c = 1,$$
$$\langle\sigma_x\rangle \sim |g - g_c|^{1/2},$$
$$\frac{\langle\sigma_z\rangle + 1}{2} \sim |g - g_c|^1,$$
$$n_c \equiv \frac{\omega_0}{\Omega}\langle a^\dagger a\rangle \sim |g - g_c|^1.$$

特别地，$g < g_c$ 时 $\langle\sigma_x\rangle$ 和 n_c，而在 $g > g_c$ 时取得了非 0 值，体现了 Z_2 对称性的破缺。

然而，实验中 $\Omega/\omega_0 \to \infty$ 显然是无法操作的，在我们的实验中，这一比值的最大可取值受到激光功率的限制。不过有限频率放缩（finite-frequency scaling, FFS）假设预测，在 $g = g_c$ 处，测定观测量随 Ω/ω_0 的变化，也能得到幂次关系：

$$\frac{\langle\sigma_z\rangle + 1}{2} \sim \left(\frac{\Omega}{\omega_0}\right)^{-2/3},$$
$$n_c \sim \left(\frac{\Omega}{\omega_0}\right)^{-2/3}.$$

这一关系可以用变分法获得，我们也进行了数值验证。同时 FFS 假设还给出，各观测量 A 的 FFS 函数 $F_A(x) \equiv \langle A\rangle |g - g_c|^{-\kappa_A}$ 作为 $x \equiv \frac{\Omega}{\omega_0}|g - g_c|^{3/2}$ 的函数时，只与 x 有关，和 Ω/ω_0 和 g 没有直接关系。画出不同 Ω/ω_0 情况下的 F_A-x 曲线应该重合，这种现象也得到了我们的数值确认。实验中要实现对量子相变的定量观测结果，基本要依赖 FFS 假设的这两条结论。

开放量子拉比模型（open quantum Rabi model）在 QRM 的基础上加上了玻色模式的耗散项，系统的演化将按照 Lindblad 主方程进行：

$$\frac{\mathrm{d}\rho}{\mathrm{d}t} = \mathcal{L}[\rho] = -\mathrm{i}[H_{\mathrm{QRM}}, \rho] + \kappa\mathcal{D}[a].$$

其中 ρ 是系统的密度矩阵，κ 是代表耗散强度的系数，$\mathcal{D}[a] = 2a\rho a^\dagger - a^\dagger a\rho - \rho a^\dagger a$ 是 Lindblad 形式的坍缩算符。开放 QRM 的理论推导无疑更加困难，但在实验上我们采取的是和非耗散系统完全相同的方法对相变进行观测的，即利用 FFS 的结论。理论指出，

开放 QRM 存在一个耗散性相变（dissipative phase transition, DPT），其临界点为

$$g_c = \sqrt{1 + \left(\frac{\kappa}{\omega_0}\right)^2}.$$

同时，FFS 预言了有限频率比情况下，临界点处有

$$\langle a^\dagger a \rangle \sim \left(\frac{\Omega}{\omega_0}\right)^{1/2}.$$

而且对于 $x \equiv \frac{\Omega}{\omega_0}|g - g_c|^2$ 和 $F_x \equiv \langle a^\dagger a \rangle |g - g_c|^1$，不同 Ω/ω_0 情况测得的 F_x-x 曲线重合。论文中用数值计算确认了这些结果。

实验上，我们尝试用Yb⁺- Ba⁺ 混合离子系统来模拟开放 QRM。其中Yb⁺ 离子用于模拟 QRM，Ba⁺ 离子作为耗散项。当使用激光冷却Ba⁺ 离子时，得到冷却的实际上是两个离子的共同振动模式，因此Yb⁺ 离子也能得到冷却，这称为协同冷却过程。

我们在实验上通过冷却中声子数的测定，得到了冷却速率，从而确定了 κ 的大小为0.195 kHz。并根据离子阱系统的实际情况，设计了模拟的参数为

$$\omega_0 = 2\pi \times 1\,\text{kHz}, \quad \Omega \sim 20\omega_0, \quad g \sim 1.$$

然而，对完整离子哈密顿量的模拟显示，该条件下的离子哈密顿量和理想的 QRM 哈密顿量有明显偏差。通过进一步的计算机模拟我们发现，这是由于离子哈密顿量近似步骤中的 Lamb-Dicke 近似的近似条件不成立导致的。Yb⁺ 离子在我们的装置中 Lamb-Dicke 参数为 0.122，是一个偏大的值，使得声子数稍大一些的时候，近似的效果就不好了。不论是 FFS 的指数还是 $F_{(x)}$-x 曲线的重合，都受到了影响而不再有效。

受到非耗散 QRM 相变实验的启发，我们讨论了寻找开放 QRM 相变定性证据的可能性。希望能够在实验中观察到因为对称性破缺而带来的在超辐射相情况下 $\langle a^\dagger a \rangle \neq 0$ 现象。然而通过数值模拟的结果我们发现，我们的冷却速率太慢，要在 Ω/ω_0 的情况下达到稳态，需要约40 ms。而受实验中所使用的355 nm激光器对Yb⁺ 离子操作时间的限制，我们的操作时间不允许超过1 ms，一般在数百s的量级。

考虑到上述的困难，该实验目前并未实现。只是对实验的可行参数进行了充分的探讨，对实验的设计进行了一定程度的分析和解释。

关键词：量子拉比模型，离子阱，量子模拟

Experimental Study on Dissipative Phase Transition in the Open Quantum Rabi Model

Zhou Zinan

Advisors: Kim Kihwan

ABSTRACT

This thesis reports an unsuccessful attempt to experimentally realize a dissipative phase transition (DPT) of the open quantum Rabi model (QRM). Still, we present in the thesis our investigation on the feasibility to observe such a phase transition.

We reviewed the QRM and its quantum phase transition (QPT) first. To experimentally simulate the phase transition of a quantum object we must have some sensible way to observe and distinguish it. For this purpose, we reviewed the finite-frequency scaling (FFS) hypothesis for the QRM. Two methods turn out to be practicable. First, we can extract a scaling law at the critical point by scanning frequency ratio, even it is finite. Second, the FFS function against a scaled coupling factor is supposed to be independent of the frequency ratio. For open QRM, which is the combination of an ordinary QRM and a dissipative term, these two methods are still valid.

Trapped-ion system is a popular choice to study quantum information and quantum simulation. By using a two-species ion trap, we can trap one $^{171}\text{Yb}^+$ and one $^{138}\text{Ba}^+$ ion in an effective harmonic potential. Then we employ the Yb$^+$ion as our QRM, which is cooled by the Ba$^+$ion through sympathetic cooling. The critical point of the DPT is dependent on the dissipation term, so we experimentally determined the cooling rate first. Then we explored the suitable parameter ranges to create an ion simulator. However, for our current experimental setup, an unfavorable Lambe-Dicke parameter, a weak cooling power, and a short Raman operation time become obstacles. It is even hardly possible to observe a qualitative evidence of the DPT due to an operation time of order $10\,\text{ms}$ – our typical operation time is only of order $100\,\text{s}$, beyond which the Yb$^+$ion gets dark for unclear reason.

KEYWORDS: quantum Rabi model, trapped-ion, quantum simulation

Contents

Chapter 1   Introduction

Quantum optics aims to study the interaction of matters and electromagnetic fields in a quantized aspect. The quantum Rabi model (QRM), which describes the interaction of a two-level system with a single bosonic mode, is perhaps the simplest system that embodies the substance of quantum optics.

For a magnetic moment in a uniform magnetic field B_0, the net force is cancelled, yet leaving a torque. The torque then elicits gyroscopic precession of the magnetic moment around the field direction, known as Larmor precession (Fig. 1.1a). When another rotating magnetic field is added, in its rotating frame, the magnetic moment will further precess around the inclined effective magnetic field at what is now known as Rabi frequency. In Fig. 1.1b we demonstrate the full cancellation case, where the fictitious field B_{fict} induced by transforming into the ratating frame exactly cancels B_0.

For atomic system, the electron spin is actually described by quantum angular momenta. I. I. Rabi first studied this problem by treating the atom as quantized and the field as a classically rotating one. We now name this series of model after him in respect of his pioneer work 85 years ago [1, 2]. However, it was later known that the electromagnetic field per se needs to be formalized with quantum theory, so strictly we need what is now called the quantum Rabi model (QRM) to investigate the atom-field interaction. The fully quantized model was first studied by Jaynes and Cummings [3] in 1963, which is actually a simplified variation of QRM by taking the rotating-wave approximation. Even on this simple model many meaningful theoretical and experimental studies are done in the past decades [4], because it insightfully captures the essence of matter-light interaction and is meanwhile easy to solve.

It is not until the recent years that the full QRM has aroused more and more attention. As advances in quantum information comes rapidly, better experimental techniques have been developed to perform qubit-oscillator coupling, which enables us to explore the strong coupling regimes where the rotating-wave approximation is no longer valid.

In this thesis focus particularly on the trapped-ion system. In a trapped-ion system, an ion is trapped in all three dimensions using time dependent electric fields. A qubit system is constructed by the internal electronic states of the ion, and the ion's harmonic motion inside the trap can be quantized as a bosonic field. The coupling between both parts are induced by lasers. In such a way we have a typical 'light-matter' interaction model. The trapped-ion
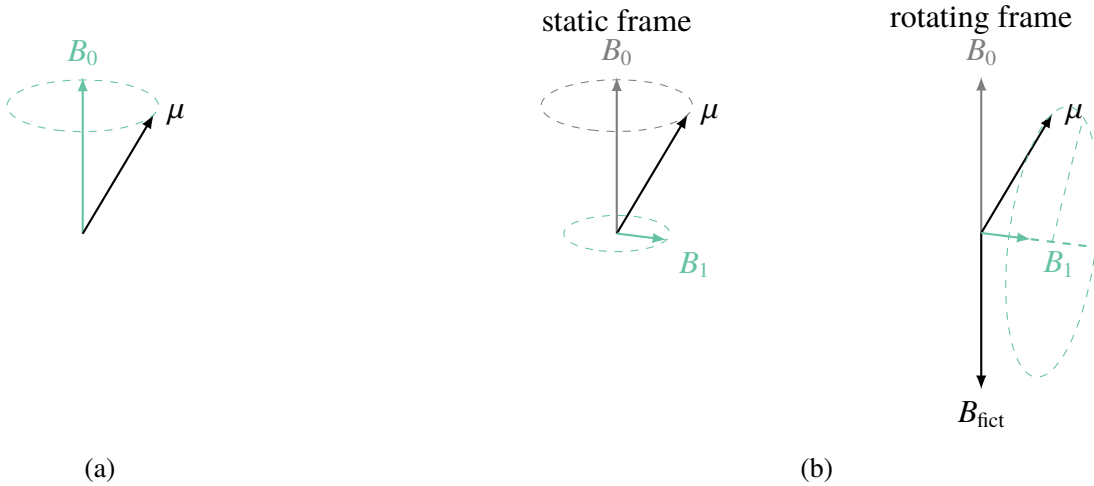
图 1.1　(a) Larmor precession of a magnetic moment in an external magnetic field B_0. (b) Rabi oscillation of a magnetic moment. A rotating magnetic field B_1 rotates apace with μ. In the rotating frame of μ, a fictitious magnetic field is induced. If it cancels B_0 exactly, the net field is B_1 and μ will rotate around B_1 at the Rabi frequency in the rotating frame.

system is noted for its long coherence time and high fidelity, which makes it a popular platform to perform quantum computation experiments. Quantum simulation, as a restricted form of quantum computation, can also be carried out with trapped ions.

The topic of this thesis is the dissipative phase transition of the open quantum Rabi model. Before starting formally we need some preliminary concepts about a quantum phase transition (QPT). One should make analogy between QPT and thermal phase transition. In a thermal phase transition the 'state' involved is an ensemble that minimizes the Gibbs free energy. A continuous thermal phase transition happens at the point where the minimum of Gibbs free energy has a discontinuity in its derivative. In a QPT the ground state energy is in place of the minimum of Gibbs free energy, and the ground state is the counterpart of a minimization ensemble.

1.1　Quantum Phase Transition

A quantum phase transition (QPT) is defined to be any point of non-analyticity in the ground states energy of the lattice system [5], where the non-analyticity could be either the limiting case of an avoided level-crossing or an actual level-crossing (Fig. 1.2).

A continuous phase transition, as the name suggests, means that the properties of the system vary continuously as the critical point is traversed. Consider the Hamiltonian $H(g) = H_0 + gH_1$, in which H_0 is a time-independent part and g is a dimensionless coupling factor.
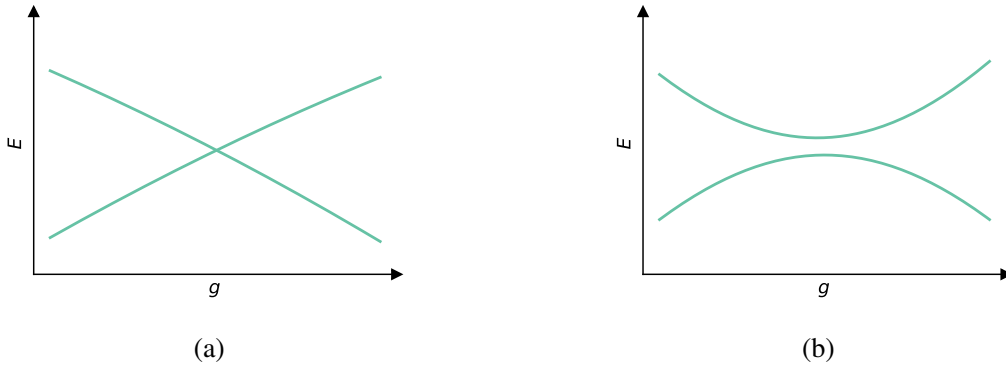
图 1.2   Ground and first-excited energy bands against the dimensionless coupling factor g. In (a) we show an actual level-crossing and in (b) an avoided one. In the limiting case where the system size gets infinitely large, the avoided crossing becomes a sharp non-analytical point and ergo indicates a quantum phase transition.

$H(1) = H_0 + H_1$ characterizes a complex system which cannot be diagonalized, but H_0 is one that we already know its eigenvalues and eigenstates. To solve the eigenstates of H, we can evolve H_0 toward $H(1)$ adiabatically, namely turn on the perturbation $g(t)$ from 0 to 1 adiabatically. In such an evolution we can usually observe energy level repulsion, resulting an avoided level-crossing like the one in Fig. 1.2b.

In some special situations, for example when H_0 commutes with H_1, it is possible to have a level-crossing: H_0 and H_1 can be simultaneously diagonalized and we can find eigenstates that is invariant with respect to g, but the energy is not and an actual crossing, say at $g = g_c$, is possible (Fig. 1.2a). When this happens, perturbation theory is no longer valid to solve H from H_0. The two sides of g_c belong to distinct phases. For a system of infinite size, there is another possibility to have a QPT: when the system size tends to infinity, an avoided-crossing could become a sharp non-analytical point.

Quantum phase transitions occur only at zero temperature $T = 0$, where the thermal fluctuations vanish and quantum fluctuations by the Heisenberg uncertainty principle dominate, so what we have discussed above are all about ground states.

We mention here basic concepts pertaining to critical exponents, which are almost the same as in a thermal phase transition and will be furnished when we review the QRM later. Continuous QPT exhibits a diverging correlation at the critical point g_c. Define a spatial correlation function for certain order parameter $\mathbf{m(r)}$ at position $\mathbf{r}$:

$$G(\mathbf{r}_1, \mathbf{r}_2) = \langle \mathbf{m(r_1)} \cdot \mathbf{m(r_2)} \rangle - \langle \mathbf{m(r_1)} \rangle \langle \mathbf{m(r_2)} \rangle$$

3

G will decay according to $G(\mathbf{r}_1, \mathbf{r}_2) \sim e^{-|\mathbf{r}_1 - \mathbf{r}_2|/\xi}$ and the correlation length ξ is given by

$$\xi^2 = \frac{\sum_{\mathbf{r}} |\mathbf{r}|^2 G(\mathbf{r}, 0)}{\sum_{\mathbf{r}} G(\mathbf{r}, 0)}$$

For a continuous QPT, ξ will diverge at the critical point

$$\xi \sim |\epsilon|^{-\nu}$$

where $\epsilon = g/g_c - 1$ so that $\epsilon_c = 0$ and ν is a positive number - the critical exponent for ξ. Similarly the critical exponents are difined for the order parameter m itself and for the relaxation time τ

$$m \sim |\epsilon|^{\beta}, \quad \tau \sim |\epsilon|^{-z\nu}.$$

1.2 Thesis Organization

This thesis is divided into the following chapters.

- Chapter 2 is about the quantum Rabi model, including its Hamiltonian and superradiant QPT. We have derived the critical exponents at the thermodynamic limit and their behavior at finite frequency ratio. Finally we come to the more sophisticated open QRM and its dissipative phase transition, which is the main research object of this thesis.

- In Chapter 3 we move to the simulation of the QRM by trapped ions. The principle and setup about our two-species ion trap system are demonstrated briefly. The we talk about the Yb⁺ion as the QRM and the Ba⁺ion as the heat bath. The procedure to experimentally work out the maximum cooling rate is illustrated. Finally we show our effort to search pragmatic experimental scheme and the constraint we face now.

- Chapter 4 contains discussions, conclusion and outlook.

- Appendices follow the main text. Detailed calculation steps and important simulation source codes are included.

Chapter 2　The Quantum Rabi Model

This chapter gives a brief introduction to the quantum Rabi model and its quantum phase transition. The core problem here is to determine what we can practically observe in experiments as phenomena of the phase transition. We derive the Hamiltonian for the QRM, as well as for its simplified version called the Jaynes-Cummings model. We skim through its basic properties about symmetry, observables and coupling regimes. Then we move to the theory about quantum phase transitions. After introducing basic concepts, we exactly diagonalized the QRM Hamiltonian in the infinite frequency ratio limit and computed the critical exponents. The case of finite frequency ratio is subsequently discussed. Finally, we consider an open QRM and its dissipative phase transition. We find that a similar methodology can be applied to investigate the open QRM.

2.1　Quantum Rabi Model

The Hamiltonian of a single-mode free field is

$$H_{\mathrm{F}} = \hbar\omega_0\left(a^\dagger a + \frac{1}{2}\right),$$

where $a^\dagger$ and a is the bosonic creation and annihilation operator respectively, satisfying $\left[a, a^\dagger\right] = 1$. ω_0 is the frequency of the bosonic mode. The eigenstates of H_{F} is number states or Fock states $|n\rangle$, $n = 0, 1, 2, \ldots$. The Hamiltonian of a two-level system, with the energy reference point set at midway of the upper and the lower level, is

$$H_{\mathrm{A}} = \frac{\hbar\Omega}{2}\sigma_z,$$

where $\hbar\Omega$ is the energy splitting, and σ_z is one of the Pauli matrices, which obey $\left[\sigma_i, \sigma_j\right] = 2\mathrm{i}\epsilon_{ijk}\sigma_k$, $i, j, k = x, y, z$. We will label the spin-up and spin-down eigenstates as $|\uparrow\rangle$ and $|\downarrow\rangle$ respectively. For simplicity we will drop the zero-point energy term in H_{F} and set $\hbar = 1$. If there is no coupling between the two systems, the non-interacting Hamiltonian is then

$$H_0 = \omega_0 a^\dagger a + \frac{\Omega}{2}\sigma_z. \tag{2.1}$$

(a) (b)
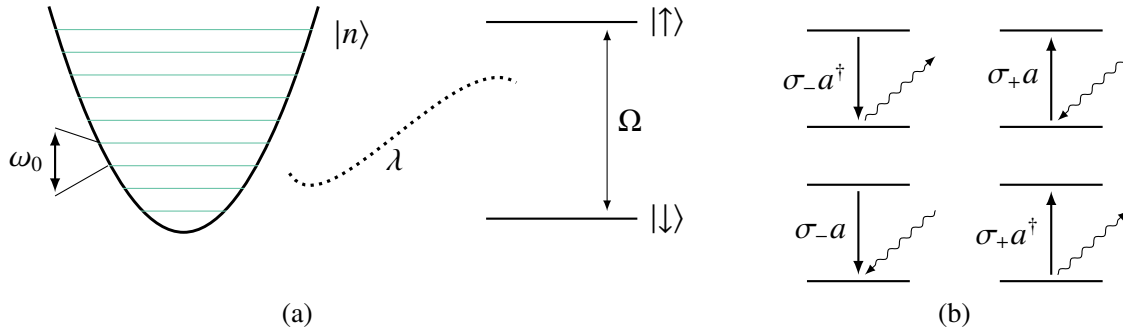
图 2.1 Schematic diagram of the quantum Rabi model. In (a) we show the components of H_{QRM}. The left side represents a single-mode bosonic field, namely a quantum harmonic oscillator. Its energy levels are known as number states or Fock states $|n\rangle$. The right side represents a two-level system, or a qubit system, whose levels are marked as $|\uparrow\rangle$ and $|\downarrow\rangle$. They are coupled through the interaction part H_1 with a strength λ. In (b) we show the four possible exchange processes contained in $(\sigma_+ + \sigma_-)(a + a^\dagger)$. The top two are rotating terms that consist of the Jaynes-Cummings model, which conserve the total excitation number N_e. In the upper right diagram for example, the qubit system gets excited from $|\downarrow\rangle$ to $|\uparrow\rangle$ by absorbing a boson from the field. The bottom two are counter-rotating terms that are dropped in rotating-wave approximation, which do not conserve N_e. They will have significant effect when λ/ω_0 gets large and cannot be neglected.

Consider a dipole interaction $H_1 = -d \cdot E$. Because $E \propto (a + a^\dagger)$ for quantized field and the dipole moment is non-vanishing only between different parity, i.e. $\langle \uparrow |d| \uparrow \rangle = \langle \downarrow |d| \downarrow \rangle = 0$. The interacting part is hence

$$\lambda H_1 = -\lambda \sigma_x (a + a^\dagger), \tag{2.2}$$

where λ characterizes the coupling strength. With the discussion above we establish the Hamiltonian for the quantum Rabi model (Fig. 2.1a):

$$H_{\text{QRM}} = \omega_0 a^\dagger a + \frac{\Omega}{2} \sigma_z - \lambda \sigma_x (a + a^\dagger). \tag{2.3}$$

Here $\sigma_x(a + a^\dagger) = (\sigma_+ + \sigma_-)(a + a^\dagger)$ contains 4 terms (Fig. 2.1b). In the interaction picture of H_0, we have

$$\sigma_+ a \propto e^{i(\Omega - \omega_0)t}, \quad \sigma_- a^\dagger \propto e^{i(\omega_0 - \Omega)t},$$

$$\sigma_+ a^\dagger \propto e^{i(\omega_0 + \Omega)t}, \quad \sigma_- a \propto e^{-i(\omega_0 + \Omega)t}.$$

Under the conditions of near-resonance and weak coupling, which means $|\omega_0 - \Omega| \ll |\omega_0 + \Omega|$ and $\lambda \ll |\omega_0 + \Omega|$, we can neglect the last two counter-rotating terms, which vary much rapidly than the first two has no average effect. After this rotating-wave approximation (RWA) we obtain a simpler model known as Jaynes-Cummings model (JCM)
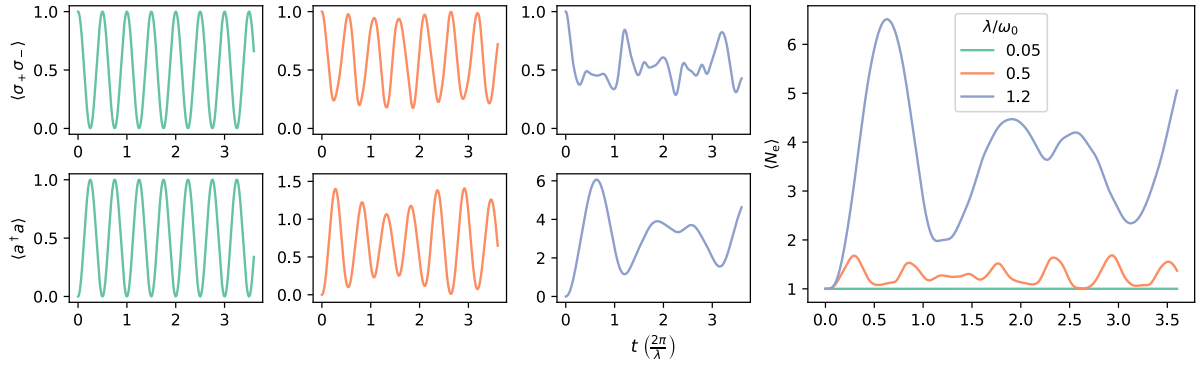
图 2.2 Spin and boson observables of QRM in different coupling regimes. The case of exact resonance $\omega_0 = \Omega$ is plotted here as an example. In the JC regime (mint green), $\langle \sigma_+ \sigma_- \rangle$ and $\langle a^\dagger a \rangle$ show standard Rabi oscillations, and the total excitation number $N_e = 1$ is conserved. In the USC regime (orange), the oscillations are distorted and $\langle a^\dagger a \rangle$ can go larger than 1. In the DSC regime (cerulean) the QRM shows a completely different behavior, $\langle a^\dagger a \rangle$ and thus $\langle N_e \rangle$ can reach very large values.

$$H_{JCM} = \omega_0 a^\dagger a + \frac{\Omega}{2} \sigma_z - \lambda \left(\sigma_+ a + \sigma_- a^\dagger \right). \tag{2.4}$$

We will simply introduce the JCM as well since it is closely related to sideband transitions, which we use to perform single-qubit operation on ions. Define the excitation number operator $N_e = a^\dagger a + |{\uparrow}\rangle\langle{\uparrow}|$, we will find out that H_{JCM} conserves the total excitation number, $[H_{JCM}, N_e] = 0$. With this conserved quantity we can decompose the Hilbert space into an infinite direct sum of two-dimensional invariant subspaces, each labeled by an eigenvalue of N_e. The subspaces are sometimes known as Jaynes-Cumming doublets. With this conserved quantity, the JCM can be analytically solved in various ways, rendering it a paradigm in almost every quantum optics textbook [6].

While the JCM has this nice $U(1)$ continuous symmetry generated by N_e, in the QRM it is broken down to only a Z_2 discrete symmetry, due to counter-rotating terms which do not conserve N_e. This mathematical complexity made the QRM once believed to be not analytically solvable, but in 2011 Braak [7] concluded that the Z_2 symmetry alone is sufficient to indicate solvability. Since then, a series of study on the analytical solution to the QRM were conducted [8, 9]. The parity operator, which generates the Z_2 symmetry, is $\Pi = e^{i\pi N_e}$, $[H_{QRM}, \Pi] = 0$. When the coupling strength is comparable to the bosonic frequency, $0.1 \lesssim \lambda/\omega_0 \lesssim 1$, it is defined as the ultrastrong coupling (USC) regime, and when $\lambda/\omega_0 \gtrsim 1$ it is the deep strong coupling (DSC) regime. Simulation results of the QRM evolving in different regimes are shown in Fig. 2.2 for an intuitive understanding.

2.2 Superradiant Quantum Phase Transition

To study the QPT in a QRM, an exact solution to the ground state can be find by perturbation theory and some transformations [10] in the limit of $\Omega/\omega_0 \to \infty$ and $\lambda/\omega_0 \to \infty$, while keeping $g = 2\lambda/\sqrt{\omega_0 \Omega}$, with g representing the dimensionless coupling. The parameter hierarchy is therefore $\omega_0 \ll \lambda \ll \Omega$. Recall that perturbation theory is valid only within one phase, so we need to calculate for phases on the opposite sides of the critical point respectively.

For the non-interacting Hamiltonina H_0 (eqn. 2.1), the boson part and the spin part is uncoupled and the Hilbert space $\mathcal{H}$ can be partitioned according to spin eigenstates, $\mathcal{H} = \mathcal{H}_\uparrow \oplus \mathcal{H}_\downarrow$. When $\omega_0 \ll \Omega$, the lowest eigenstates are confined in $\mathcal{H}_\downarrow$. The inclusion of λH_1 of course causes coupling between these two subspaces, altering the behavior of the ground state energy. To fix this problem and make the matrix of H diagonal again with respect to the spin basis $\{|\uparrow\rangle, |\downarrow\rangle\}$, we can do the perturbative expansion as a unitary transformation S [11, Chapter 6]. Assume S is of order λ and has zero diagonal. By Baker-Hausdorff formula

$$
\begin{aligned}
\mathrm{e}^{iS} H_{\mathrm{QRM}} \mathrm{e}^{-iS} &= H_{\mathrm{QRM}} + i\left[S, H_{\mathrm{QRM}}\right] + \frac{1}{2}\left[iS, \left[iS, H_{\mathrm{QRM}}\right]\right] \\
&= H_0 - \lambda H_1 + [iS, H_0] + [iS, -\lambda H_1] + \frac{1}{2}[iS, [iS, H_0]] + O(\lambda^3)
\end{aligned}
\tag{2.5}
$$

The first term is of order λ^0 and is diagonal; the second and third term is of order λ^1 and is off-diagonal. Our desirable S is the one that cancels the off-diagonal terms, namely

$$
[iS, H_0] = \lambda H_1,
$$

which gives

$$
S = -\frac{\lambda}{\Omega}\left(a + a^\dagger\right)\sigma_y = -\frac{g}{2}\sqrt{\frac{\omega_0}{\Omega}}\left(a + a^\dagger\right)\sigma_y.
$$

And we can check:

$$
[iS, H_0] = \left[-\frac{i\lambda}{\Omega}\left(a + a^\dagger\right)\sigma_y, \omega_0 a^\dagger a + \frac{\Omega}{2}\sigma_z\right] = \frac{i\omega_0\lambda}{\Omega}\left(a^\dagger - a\right)\sigma_y + \lambda\left(a + a^\dagger\right)\sigma_x,
$$

which equals λH_1 since ω_0/Ω tends to zero. Substitute S into (2.5) then

$$
\mathrm{e}^{iS} H_{\mathrm{QRM}} \mathrm{e}^{-iS} = \omega_0 a^\dagger a + \frac{\Omega}{2}\sigma_z + \frac{\omega_0 g^2}{4}\left(a + a^\dagger\right)^2 \sigma_z + \frac{\omega_0 g^3}{6}\sqrt{\frac{\omega_0}{\Omega}}\left(a + a^\dagger\right)^3 \sigma_x + O\left(\frac{\omega_0}{\Omega}\right).
$$

The term $\left(a + a^\dagger\right)^2 \sigma_z$ is of order (ω_0/Ω) and is diagonal. Thus in the limit of $\Omega/\omega_0 \to \infty$, we

have a transformed Hamiltonian that is diagonal up to order $\sqrt{\omega_0/\Omega}$

$$H' = \omega a^\dagger a + \frac{\Omega}{2}\sigma_z + \frac{\omega_0 g^2}{4}\left(a + a^\dagger\right)^2 \sigma_z.$$

The lowest eigenstates in $\mathcal{H}_\downarrow$ is now contained in

$$H_{\mathrm{np}} = \langle\downarrow|H'|\downarrow\rangle = \omega_0 a^\dagger a - \frac{\omega_0 g^2}{4}\left(a + a^\dagger\right)^2 - \frac{\Omega}{2}. \tag{2.6}$$

Finally, we resort to the well-known Bogoliubov transformation to 'diagonalize' H_{np} [12], namely to clear out the non-particle-number-conserving terms a^2 and $\left(a^\dagger\right)^2$. Apply the squeeze operator $\mathcal{S}(-r) = \exp\left[-\frac{r}{2}\left(a^2 - a^{\dagger 2}\right)\right]$ onto H_{np}, we have (See A.2).

$$H_{\mathrm{np}} = \omega_0\sqrt{1 - g^2}a^\dagger a + E_{\mathrm{G,np}}(g), \tag{2.7}$$

where $E_{\mathrm{G,np}}(g) = \omega_0\left(\sqrt{1 - g^2} - 1\right)/2 - \Omega/2$ is the ground state energy. For the expression above it is evident that the effective Hamiltonian H_{np} is valid only for $0 \leq g \leq 1$. To calculate the $g > 1$ case we first transform H_{QRM} with a displacement operator $\mathcal{D}(\alpha) = \exp\left(\alpha a^\dagger - \alpha^* a\right)$ and a rotation in the spin subspace [13] (See A.3). The resulting superradiant phase effective Hamiltonian is

$$H_{\mathrm{sp}} = \omega_0\sqrt{1 - g^{-4}}a^\dagger a + E_{\mathrm{G,sp}}(g),$$

$$E_{\mathrm{G,sp}}(g) = \omega_0\left(\sqrt{1 - g^{-4}} - 1\right)/2 - \Omega(g^2 + g^{-2})/4$$

As the transfromed Hamiltonians have number states as their eigenstates, we can derive the eigenstates before transformation.

$$\left|\psi_{\mathrm{np}}^n\right\rangle = \mathcal{S}\left(-r_{\mathrm{np}}\right)|n\rangle|\downarrow\rangle,$$

$$\left|\psi_{\mathrm{sp}}^n\right\rangle = \mathcal{D}\left(\pm\alpha_g\right)\mathcal{S}\left(-r_{\mathrm{sp}}\right)|n\rangle\left|\downarrow^\pm\right\rangle.$$

Explanation of parameters is shown below:

$$r_{\mathrm{np}} = -\frac{1}{4}\ln\left(1 - g^2\right), \qquad\qquad r_{\mathrm{sp}} = -\frac{1}{4}\ln\left(1 - g^{-4}\right),$$

$$\alpha_g = \sqrt{\frac{\Omega(g^4 - 1)}{4g^2\omega_0}}, \qquad\qquad \left|\downarrow^\pm\right\rangle = \mp\sqrt{\frac{1 - g^{-2}}{2}}|\uparrow\rangle + \sqrt{\frac{1 + g^{-2}}{2}}|\downarrow\rangle.$$

Notice that $\left|\psi_{\mathrm{sp}}^n\right\rangle$ is doubly degenerate in the spin subspace.

2.2.1 Critical Phenomena

Once we have computed the ground states of H_{np} and H_{sp}, we can study the behavior of observables when varying g. Specifically we are interested in the spin expectation values $\langle\sigma_x\rangle$, $\langle\sigma_z\rangle$ and the bosonic expectation value $\langle a^\dagger a\rangle$, which are experimentally feasible observables.

To compute $\langle\sigma_z\rangle$, the bosonic part turns to be completely irrelevant

$$
\begin{aligned}
\langle\psi^0_{\mathrm{np}}|\sigma_z|\psi^0_{\mathrm{np}}\rangle &= \langle\downarrow|\sigma_z|\downarrow\rangle = -1, \\
\langle\psi^0_{\mathrm{sp}}|\sigma_z|\psi^0_{\mathrm{sp}}\rangle &= \langle\downarrow^\pm|\sigma_z|\downarrow^\pm\rangle = \frac{1-g^{-2}}{2} - \frac{1+g^{-2}}{2} = -\frac{1}{g^2}.
\end{aligned}
$$

The critical exponent of $\frac{\langle\sigma_z\rangle+1}{2}$ is $\kappa_{\sigma(z)} = 1$, because

$$
\frac{\langle\sigma_z\rangle+1}{2} = \frac{(g-1)(g+1)}{2g^2} \sim |g-1|^1.
$$

Similarly,

$$
\begin{aligned}
\langle\psi^0_{\mathrm{np}}|\sigma_x|\psi^0_{\mathrm{np}}\rangle &= 0, \\
\langle\psi^0_{\mathrm{sp}}|\sigma_x|\psi^0_{\mathrm{sp}}\rangle &= \mp\sqrt{1-g^{-4}}, \\
\kappa_{\sigma(x)} &= \frac{1}{2}.
\end{aligned}
$$

Especially, $\langle\sigma_x\rangle \neq 0$ for $g > 1$ indicates a break in Z_2 symmetry, because any states with Z_2 symmetry should have vanishing $\langle\sigma_x\rangle$. For bosonic observable let's explore $n_c = \frac{\omega_0}{\Omega}\langle a^\dagger a\rangle$, which is the boson number with a normalization:

$$
\begin{aligned}
\langle\psi^0_{\mathrm{np}}|a^\dagger a|\psi^0_{\mathrm{np}}\rangle &= \langle 0|\mathcal{S}^\dagger(-r_{\mathrm{np}})a^\dagger a\mathcal{S}(-r_{\mathrm{np}})|0\rangle \\
&= \langle 0|\mathcal{S}^\dagger(-r_{\mathrm{np}})a^\dagger \mathcal{S}^\dagger(-r_{\mathrm{np}})\mathcal{S}(-r_{\mathrm{np}})a\mathcal{S}(-r_{\mathrm{np}})|0\rangle \\
&= \langle 0|\left(a^\dagger\cosh r_{\mathrm{np}} - a\sinh r_{\mathrm{np}}\right)\left(a\cosh r_{\mathrm{np}} - a^\dagger\sinh r_{\mathrm{np}}\right)|0\rangle \\
&= \langle 0|aa^\dagger\sinh^2 r_{\mathrm{np}}|0\rangle \\
&= \frac{\cosh(2r_{\mathrm{np}}) - 1}{2},
\end{aligned}
$$
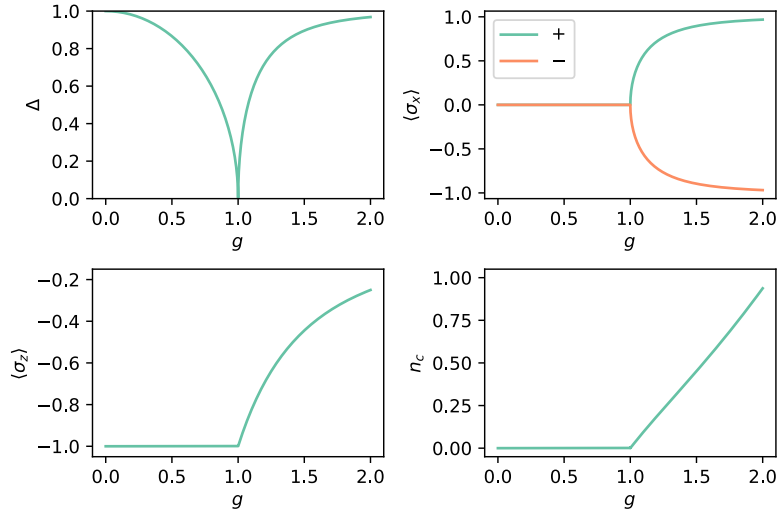
图 2.3   Energy gap between neighboring energy levels and ground state expectation values $\langle\sigma_x\rangle, \langle\sigma_z\rangle, n_c$ near the critical point $g_c = 1$. In the upper right plot the curve '+' and '−' correspond to $|\downarrow^+\rangle$ and $|\downarrow^-\rangle$ respectively; in the other plots curves for both degenerate states coincide.

where we have used (A.4) and (A.5). Conduct a similar calculation for $\left|\psi_{sp}^0\right\rangle$, the result is

$$\frac{\omega_0}{\Omega}\left\langle\psi_{sp}^0\left|a^\dagger a\right|\psi_{sp}^0\right\rangle = \frac{g^2 - g^{-2}}{4} + \frac{\omega_0}{\Omega}\frac{\cosh(2r_{sp}) - 1}{2}.$$

And it suggests that

$$n_c \sim g^2 - g^{-2} = \frac{1}{g^2}(g^2 + 1)(g + 1)(g - 1) \sim |g - 1|^1,$$

namely $\kappa_{nc} = 1$.

In Fig. 2.3 we plot the relationship between observables and g in the vicinity of its critical value $g_c = 1$. The energy gap Δ between neighboring eigenstates are also plotte, which clearly displays a QPT at g_c as $\Delta = 0$.

2.2.2   Finite-Frequency Scaling

The discussion above regarding critical exponents is valid when Ω/ω_0 tends to infinity, but in experiments we of course cannot have an infinitive Ω, which is limited by the intensity of the driving laser beam. (See Sec. 3.2.1) Luckily we still have the finite-frequency scaling (FFS) hypothesis that allows us to study critical features with finite Ω [14, 10].

FFS hypothesis is a counterpart to the finite-size scaling theory for a lattice system. Consider an $L \times L$ lattice with $N = L^2$ sites, phase transitions occur only in the thermodynamic

limite $L, N \rightarrow \infty$. For a heuristic understanding we could consider the partition function $Z = \sum_S \mathrm{e}^{-\beta H(S)}$ of the system, S stands for states. As $N \rightarrow \infty$ we must have an infinite number of states, and for an infinite summation even if H is continuous, Z and thus the expectation value of observables are not necessarily continuous, rendering non-analytical or critical points. But for a finite summation, everything is intrinsically continuous and no phase transition can ever occur (Fig. 2.4a).

Luckily finite-size scaling theory allows us to study critical behaviors as the system scale increases, going as follows. Define a scaled length $x = L/\xi$, the the microscopic details of the system is dropped within the range ξ. Suppose for an observable A, which show $A = A_0|\epsilon|^\kappa$ in the thermodynamic limit, there exists a finite-scaling function F_A such that

$$A(L) = A_0|\epsilon|^\kappa F_A(x). \tag{2.8}$$

$F(x)$ is a function of x alone and is defined only with asymptotic conditions $\lim_{x\to\infty} F_A(x) = 1$ and $\lim_{x\to 0} F_A(x) \sim x^{-\kappa/\nu}$. For an infinite lattice $L \rightarrow \infty$, equation (2.8) reduces to $A = A_0|\epsilon|^\kappa$; for a finite L, at the critical point, since ξ diverges $x \rightarrow 0$ and thus

$$A(L) \sim |\epsilon|^\kappa F_A(x) \sim L^{-\kappa/\nu}, \tag{2.9}$$

where $\xi \sim |\epsilon|^\nu$ is used. This implies the critical behavior of an infinite system can be inferred by scaling up a corresponding finite system. Note that the FFS theory is based on the leading order in $1/L$, it is valid only for sufficiently large L. Basically we have two ways to demonstrate the validity of finite-size scaling theory:

1. Plot L-$A(L)$ on a logarithmic axis. A straight line with tangent $-\kappa/\nu$ is expected.
2. Plot x-$A(L)/|\epsilon|^\kappa$ with different (ϵ, L) pairs. These curves are supposed to collapse into a single one because $F_A(x)$ is independent from L and ϵ alone. It is only dependent on their ratio x.

The good thing for our QRM is that, the ratio Ω/ω_0 functions as the system size L in the superradiant phase transition [13], which is much friendlier to experiments than making a huge system. We can adapt equation (2.9) to

$$\langle A \rangle (\Omega/\omega_0, g_c) \sim \left(\frac{\Omega}{\omega_0}\right)^{\delta_A}. \tag{2.10}$$

δ_A is equivalent to $-\kappa_A/\nu$. Surely for a system without spatial dimension it is hard to interpret
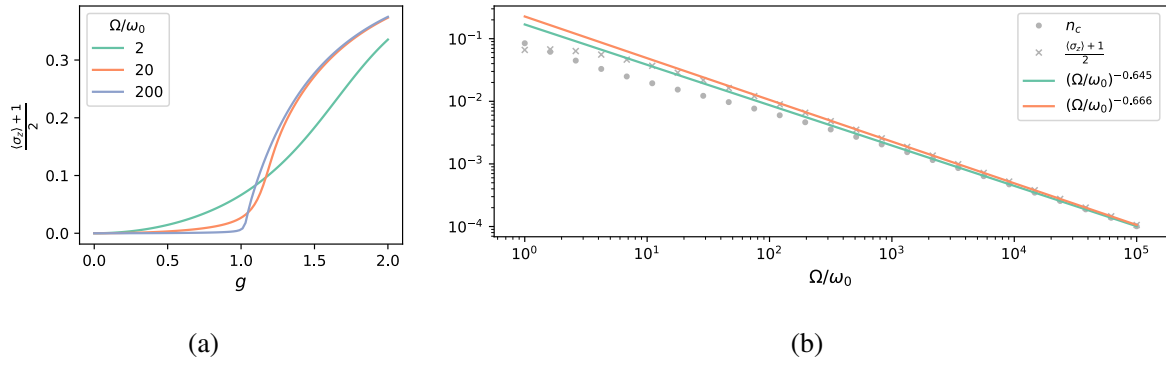
图 2.4   Expectation values of finite frequencies. (a) shows how the turning point of $\frac{\langle\sigma_z\rangle+1}{2}$ flattens out as Ω/ω_0 becomes small. (b) shows the scaling of n_c and $\frac{\langle\sigma_z\rangle+1}{2}$ with respect to Ω/ω_0 at the critical point $g_c = 1$. Deviation from the power law can be observed, especially for n_c which is affected by correction terms of order $(\Omega/\omega)^1$.

the meaning of ξ and its critical exponent ν, but since we have calculated κ_A for σ_z and n_c, we can always obtain $\delta_{\sigma(z)}$ and δ_{nc} by fitting experimental data, and examine whether a common ν exists. If that is true, we can again define $x = |g - g_c|^\nu \Omega/\omega_0$. Similarly, we expect $A/|g - g_c|^\kappa$ is the same for all $(g, \Omega/\omega_0)$ pairs while keeping x.

In Fig. 2.4b we plot the relation (2.10) for n_c and $\frac{\langle\sigma_z\rangle+1}{2}$ obtained by numerical calculation and fit their exponents δ. When Ω/ω_0 goes large, an increasing number of Fock states $|n\rangle$ are involved, so in this simulation we have to truncate the Fock space at a rather large n. Here we have chosen $n = 300$ which is large enough for Ω/ω_0 up to 10^5. The fitting is done within the range 10^4 to 10^5 to avoid the impact from higher order terms. Despite a small distinction between the two lines, it is strongly suggested that $\delta_{\sigma(z)}$ and δ_{nc} are both $-2/3$. Since their critical exponents are both 1, a common ν does exist with value $3/2$. The exponents here can actually be verified by applying variational methods to the ground states and extract the leading order terms of Ω/ω_0 [13].

Then we can verify the FFS functions are invariant for different values of g and Ω/ω_0. By numerically solving H_{QRM} for various Ω/ω_0 and g it is easy to derive the FFS functions from expectation values. In Fig. 2.5 we plot $F_{nc}(x)$ and $F_{\sigma(z)}(x)$ against $x = \Omega/\omega_0|g - g_c|^{3/2}$. We could identify a $F(x)$ on both sides of g_c. It is clear that collections of points belonging to four Ω/ω_0 values collapse into a single curve, as the FFS hypothesis indicates.

13
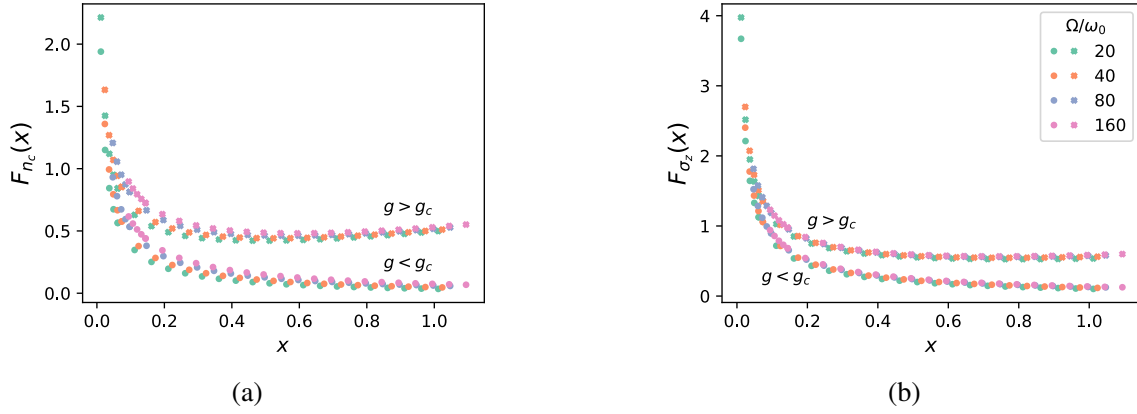
图 2.5   Finite-frequency scaling functions for n_c and $\frac{\langle\sigma_z\rangle+1}{2}$. The horizontal axis represents the scaled length $x = \frac{\Omega}{\omega_0}|g - g_c|^{3/2}$ and the vertical axis represents $F_A(x) = \langle A\rangle |g - g_c|^{-\kappa}$ for $A = n_c, \frac{\langle\sigma_z\rangle+1}{2}$ respectively.

2.3   Dissipative Phase Transition

Unlike electron systems in condensed matter physics, quantum optical systems have an intrinsic open nature. In other words, there are losses everywhere when we manipulate such a system. If the dissipation is controllable, it allows us to probe non-equilibrium phenomena.

Hwang et al. [15] have proved the existence of a dissipative phase transition (DPT) in an open QRM. The open QRM is a QRM whose boson part is a damped harmonic oscillator. Its time evolution is then depicted by the Lindblad master equation [16]

$$\frac{\mathrm{d}\rho}{\mathrm{d}t} = \mathcal{L}[\rho] = -\mathrm{i}\big[H_{\mathrm{QRM}}, \rho\big] + \kappa\mathcal{D}[a]. \tag{2.11}$$

where H_{QRM} is the same as in equation (2.3), κ is the damping rate, and $\mathcal{D}[a] = 2a\rho a^\dagger - a^\dagger a\rho - \rho a^\dagger a$ is the collapse operator a in the Lindblad form.

Despite the complexity of DPT theories, our focus regarding experimental observation is similar as that of a QPT: the scaling with Ω/ω_0 at g_c and the x-dependency of $F_A(x)$. The theoretical derivation of the DPT, its critical behavior, the scaling exponents, is far beyond the scope of this thesis and here we simply cite the results from Hwang et al. [15]. Also, since our simulation discovers that $n = a^\dagger a$ is the only good observable within experimentally feasible parameter ranges, so within this section we will only present results regarding it.

Due to the dissipation, the critical point is shifted from 1 to

$$g_c = \sqrt{1 + \frac{\kappa^2}{\omega_0^2}}.$$

(a)   (b)
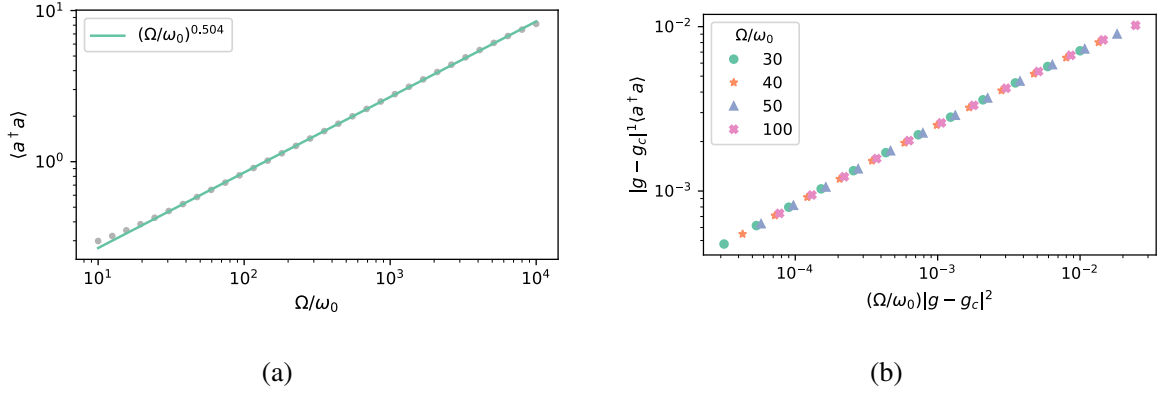
图 2.6   Finite-frequency relations of $\langle a^\dagger a \rangle$ for the DPT of the QRM. In (a) we show the scaling at g_c in respect of Ω/ω_0. A straight line of slope 0.504 is fitted for Ω/ω_0 from 10^2 to 10^5, validating the theoretical result 1/2. In (b) the FFS function for four different frequencies are plotted. In computation the Fock space is truncated at $n = 200$ and $n = 100$ respectively for (a) and (b).

Still, we have the system in the normal phase for $g < g_c$ and in the superradiant phase for $g > g_c$. In the limit of $\Omega/\omega_0 \to \infty$, we have

$$\langle a^\dagger a \rangle \sim |g - g_c|^{-1},$$

where the expectation is now calculated in respect of the steady state, which is analogous to the ground state in a QPT. For finite frequencies, we have

$$\langle a^\dagger a \rangle \sim \left(\frac{\Omega}{\omega_0} \right)^{\frac{1}{2}}$$

at $g = g_c$. Notice again this scaling is only valid for rather large Ω/ω_0 values. In Fig. 2.6a we demonstrate the numerical simulation result for this scaling and fit the exponent from within the range 10^2 to 10^4. In Fig. 2.6b we see $F_{a^\dagger a}(x)$ indeed collapse into a single curve for distinct frequencies.

Chapter 3　　Experiments with Trapped-Ions

In this chapter we introduce our experimental setup: how the ions get trapped and how they are generally used as qubits. To simulate an open QRM, we employ a Yb$^+$ion as the simulator and a Ba$^+$ion as the dissipation term. We experimentally determined the cooling parameter κ, and considered parameters that are suitable to conduct the experiment. Although an actual experiment cannot be achieved yet due to limitation on hardware, we search for possibilities to have further experimental study in this direction. When we quote angular frequency values like ω_0, we will often write explicitly $\omega = 2\pi \times 1\,\mathrm{MHz}$ rather than $\omega_0 = 6.28 \times 10^6\,\mathrm{Hz}$ to avoid ambiguity. It should not be confused with laboratory frequencies $f_0 = \omega_0/(2\pi)$. And we will express decay rates as inverse times in angular frequency units: $\mathrm{e}^{-\gamma t}$ where $\gamma = 10^4\,\mathrm{s}^{-1}$ for instance, meaning $\tau = 1/\gamma = 100\,\mathrm{s}$.

3.1　Paul Trap

We know from Gauss's law that for a static electric field $\boldsymbol{\nabla} \cdot \mathbf{E} = 0$ in a charge-free space. In other words, Laplace's equation $\nabla^2 V = 0$ does not allow any local extremum inside the boundary. Consequently we cannot trap a charged particle in all three dimensions solely with static electric fields. A typical solution for trapped-ion system is to apply an oscillating electric field, which takes advantage of the inertia of ions and creates an effective trapping in all dimensions.

Consider a general potential which is quadrapolar at the center

$$V(x,y,z,t) = \frac{U}{2}\big(\alpha x^2 + \beta y^2 + \gamma z^2\big) + \frac{\tilde{U}}{2}\cos(\omega_{\mathrm{rf}}t)\big(\alpha' x^2 + \beta' y^2 + \gamma' z^2\big). \tag{3.1}$$

The first term is static and the second is sinusoidal at radiofrequency (rf) drive frequency ω_{rf}. Gauss's law then tells

$$\alpha + \beta + \gamma = 0,$$
$$\alpha' + \beta' + \gamma' = 0.$$

The choice used in linear traps, also known as Paul traps, is

$$\gamma = -(\alpha + \beta) > 0,$$

$$\alpha' = -\beta', \quad \gamma' = 0.$$

This configuration leads to a dynamical confinement in the x-y plane and a static one in the z direction. A particle with charge $Z|e|$ and mass m in such a potential will have its equation of motion, say along the x-axis.

$$\frac{d^2 x}{dt^2} = -\frac{Z|e|}{m} \left[U\alpha + \tilde{U} \cos(\omega_{rf} t)\alpha' \right] x.$$

Equations of motion for other degrees of freedom all have a similar form. With substitutions

$$\xi = \frac{\omega_{rf} t}{2}, \quad a_x = \frac{4Z|e|U\alpha}{m\omega_{rf}^2}, \quad q_x = \frac{2Z|e|\tilde{U}\alpha'}{m\omega_{rf}}$$

we get the standard form of the Mathieu equation

$$\frac{d^2 x}{d\xi^2} + [a_x - 2q_x \cos(2\xi)]x = 0. \tag{3.2}$$

In the case $|a_x|, q_x^2 \ll 1$, we have an approximate solution [17]

$$x = x_0 \cos\left(\frac{\beta_x}{2}\omega_{rf} t\right) \left[1 - \frac{q_x}{2}\cos(\omega_{rf} t)\right], \quad \beta_x = \sqrt{a_x + \frac{q_x^2}{2}}. \tag{3.3}$$

This solution is a superposition of two oscillating terms at distinct frequencies. The major part of x is a slowly oscillating term at frequency $\nu = \beta_x \omega_{rf}/2$, which is called the secular motion. The small but fast oscillating term at rf frequency is called the micromotion. If the micromotion can be neglected, the motion of the particle is no more than a harmonic oscillator at frequency ν.

We know that a harmonic oscillator can be described in a quantum-mechanical picture. Suppose x is now the position operator of the ion, then the motional energy is given by

$$H_{\text{motion}} = \nu\left(a^\dagger a + \frac{1}{2}\right), \quad x = \sqrt{\frac{1}{2m\nu}}(a + a^\dagger)$$

which contributes to the second term in (3.4). If n ions are in the trap, there will be in total $3n$
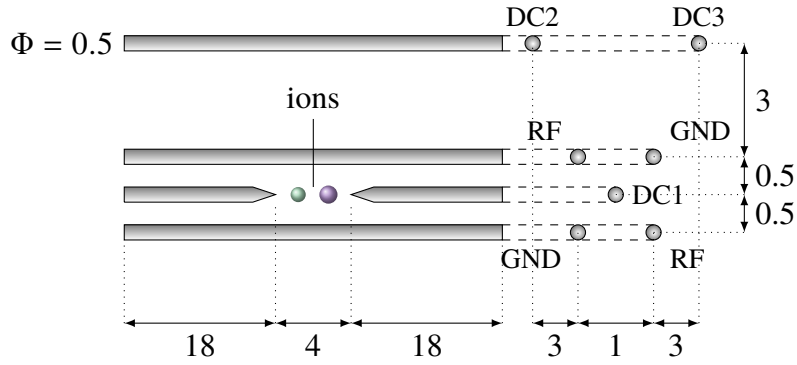
图 3.1　Schematic drawing of the linear trap. Rods labelled with 'RF' applies the rf potential $\tilde{U}\cos(\omega_{\mathrm{rf}}t)$, and all other rods are connected to rf ground. Rod 'DC1' applies the DC potential U. Rods 'DC2' and 'DC3' are for compensation of micromotion. Rod diameters and distances are shown in unit mm and are not-to-scale in the drawing above.

distinct motional modes. We can couple one particular mode out of them to the internal states by tuning laser frequencies. This motional mode is sometimes called the 'bus mode' since it transports information between ion qubits.

In our experiments, we use a traditional 4-rod trap (Fig. 3.1) made of stainless steel. The four parallel rods locate at the corners of a square, generating the rf field. Two needle DC electrodes are placed along the axis through the center, imposing trapping along the axial direction. Two auxiliary DC electrodes are employed to compensate micromotion. Typical electric field parameters in experiments are: $\tilde{U}$ =700–800V, $|U|$ =0–10V, ω_{rf} = $2\pi\times$(10–30)MHz.

3.2　Ytterbium Ion: the QRM

It is very natural that a Paul trap can restrain multiple species of ions. They are all charged particles, after all. To become a genuine 'hybrid ion trap', it means our system contains lasers that can drive transitions needed for both species of ions: single qubit rotation, coupling to the shared motional mode, etc. In our DPT experiment we employ the Yb⁺ion as the QRM and the Ba⁺ion as a heat bath. Therefore, only the quantum nature of Yb⁺ion is pertinent.

[171]Yb⁺ ion is a popular choice to perform quantum computation. It has a 1/2 nuclear spin which generates hyperfine splittings. We use the ground state hyperfine levels $|F = 0, m_F = 0\rangle$ and $|F = 1, m_F = 0\rangle$, known as 'clock' states, to encode $|\downarrow\rangle$ and $|\uparrow\rangle$ respectively. The energy gap between them is 12.642 812 118 466 GHz at zero magnetic field. They have extremely long lifetime and are first-order insensitive to magnetic field at $B = 0$. While these features make [171]Yb⁺ a favored candidate to serve as a qubit, the price we need to pay is its complex
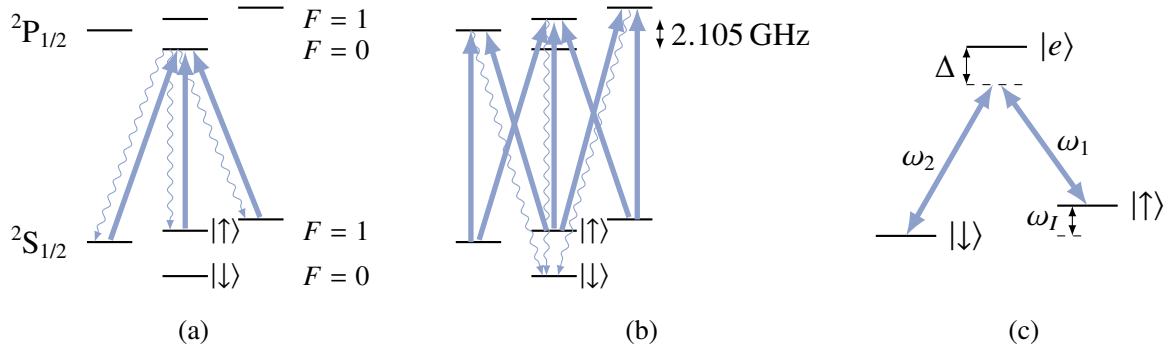
图 3.2   (a) Detection of the spin states. $|\uparrow\rangle$ is excited by a near resonant detection beam at 369.5 nm, and soon decays spontaneously to $^2S_{1/2}$ Zeeman states, emitting fluorescence. (b) Optical pumping to the $|\downarrow\rangle$ state. The state $|\uparrow\rangle$ gets exited to one of $^2P_{1/2}|F = 1, m_F = 0, \pm 1\rangle$ states, and then spontaneously decays to both $|\uparrow\rangle$ (not shown) and $|\downarrow\rangle$. $|\downarrow\rangle$ cannot be excited and the ion gets trapped there. In (a) and (b) the bold arrows represent stimulated absorption; the snake arrows represent spontaneous emission. (c) Λ-type stimulated Raman transition. $|\uparrow\rangle$ and $|\downarrow\rangle$ are coupled by two beams via a virtual state $|e\rangle$. Energy levels shown are not-to-scale.

level structure: a lot of lasers are involved in our system to manipulate it.

3.2.1   Standard Experimental Procedure

Before manipulation on qubit states, we need to prepare an initial state. The initialization process includes cooling and optical pumping.

First, Doppler cooling is performed between $^2S_{1/2}$ and $^2P_{1/2}$ manifolds with a beam at a wavelength $\lambda = 369.5$ nm. The laser beam is slightly red detuned from resonance, so an ion moving towards the light source has a higher absorption probability. On the other hand, when the excited ion emits the photon back by spontaneous emission, the direction of the photon is random. After many repetition the cooling cycle, the average momentum of the ion gets reduced. The final average phonon number after Doppler cooling is around 10. To further reduce this value a resolved sideband cooling is performed subsequently. It is a combination of red sideband transition and optical pumping, which we will introduce later.

The cooling process brings the ion to its motional ground state $|0\rangle$. To initialize the qubit state we resort to the optical pumping technique. The 369.5 nm beam which couples $^2S_{1/2}|F = 1, m_F = 0\rangle$ to $^2P_{1/2}|F = 0, m_F = 0\rangle$ is now modulated by 2.105 GHz using an electro-optic modulator (EOM), so that it can couple the $^2S_{1/2}|F = 1, m_F = 0\rangle$ state to the $^2P_{1/2}|F = 1, m_F = 0, \pm 1\rangle$ states, which can then decay to $|\downarrow\rangle$ (Fig. 3.2b). Despite the undesired possibility of decaying to the $|\uparrow\rangle$ state, because the $|\downarrow\rangle$ state cannot be excited due to the 12.6 GHz detuning, eventually all the population is removed to $|\downarrow\rangle$.

We couple $|\uparrow\rangle$ and $|\downarrow\rangle$ (and also spin states and motional states, as discussed later) with a

stimulated Raman transition. The ground states $|\uparrow\rangle$ and $|\downarrow\rangle$ are coupled to another short-lived excited state $|e\rangle$ by two lasers detuned from each other by the qubit splitting and both detuned from $|e\rangle$ (Fig. 3.2c). When detuning from $|e\rangle$ is sufficiently large, the population of $|e\rangle$ can be adiabatically removed and an effective two-level coupling can be realized. The effective frequency, wave vector, and Rabi frequency of the stimulated Raman transition is given by [17, 18]

$$\omega = \omega_1 - \omega_2, \quad \mathbf{k} = \mathbf{k}_1 - \mathbf{k}_2, \quad \Omega_R = \frac{|\Omega_{R1}\Omega_{R2}|}{2\Delta}.$$

In experiments, we can control the frequency difference precisely using acousto-optical modulators, and can change $\mathbf{k}$ by adjusting the angle between two Raman beams. In later calculation we will mostly use the effective two-level model for simplicity.

Finally we need to detect the spin states after finishing an experiment. It is carried out by a spin dependent fluorescent technique. We use a near resonant detection beam at 396.5 nm to couple $|\uparrow\rangle$ and $^2\mathrm{P}_{1/2}|\mathrm{F} = 0, \mathrm{m_F} = 0\rangle$. The latter state then spontaneously decays to one of the three $^2\mathrm{S}_{1/2}|\mathrm{F} = 1, \mathrm{m_F} = 0, \pm 1\rangle$ Zeeman states after about 10 ns (Fig. 3.2b). The emitted fluorescent photons will be collected by a photomultiplier tube (PMT) or a charge-coupled device (CCD). The detection beam contains all polarization components in order to excite the Zeeman states again. Since the $|\downarrow\rangle$ state, which we call the dark state is neither excited nor populated by decaying, the amount of fluorescent photons reflects the population in $|\uparrow\rangle$, which we call the bright state.

3.2.2 Trapped-Ion Hamiltonian and Everyday Operations

The trapped-ion Hamiltonian has components that are very similar to that of a QRM (2.3), except that the bosonic field is now made up of motional exitation quanta, i.e. phonons. Thus we can write down the non-interacting part easily

$$H_0 = \frac{\omega_I}{2}\sigma_z + \nu a^\dagger a,$$

in which ω_I is the frequency separation between $|\uparrow\rangle$ and $|\downarrow\rangle$ and ν is the motional mode frequency. What is different lies in the interaction part. Note that although we use lasers to couple the internal part and the motional part, our boson field is the quantized harmonic motion rather than the electromagnetic field. In all cases we treat the electromagnetic fields as classical plane waves:

$$\mathbf{E}(\mathbf{r}, t) = \mathbf{E}_0 \big[e^{i(\mathbf{k}\cdot\mathbf{r} - \omega_F t - \phi)} + \text{c.c.} \big]$$

The dipole interaction is therefore

$$H_1 = \frac{\Omega}{2}\sigma_x\left[e^{i(\mathbf{k}\cdot\mathbf{r}-\omega_F t-\phi)} + \text{c.c.}\right]$$

Here Ω is the (resonance) Rabi frequency, which is dependent on the intensity of the driving laser. Suppose there are multiple beams acting simultaneously, the interaction term should be a summation of them all. We reach the full Hamiltonian of a trapped-ion:

$$H_{\text{ion}} = \frac{\omega_I}{2}\sigma_z + \nu a^\dagger a + \sum_j \frac{\Omega_j}{2}\sigma_x\left[e^{i(\mathbf{k}_j\cdot\mathbf{r}-\omega_j t-\phi_j)} + \text{h.c.}\right] \tag{3.4}$$

The full Hamiltonian is rather complicated and we need to introduce some routine approximations for H_{ion}. From now on we will only consider the vibration along x direction for simplicity, $\mathbf{k}_j \cdot \mathbf{r} = k_j x$. Define the Lamb-Dicke parameter $\eta_j = k_j/\sqrt{2m\nu}$, then $k_j x = \eta_j(a + a^\dagger)$. The interaction picture Hamiltonian is given by

$$H_{\text{ion}}^I = e^{-iH_0 t}H_1 e^{iH_0 t} = \sum_j \frac{\Omega_j}{2}\left(\sigma_+ e^{i\omega_I t} + \sigma_- e^{-i\omega_I t}\right)\left[e^{i\eta_j\left(ae^{-i\nu t}+a^\dagger e^{i\nu t}\right)}e^{-i\omega_j t}e^{-i\phi_j} + \text{h.c.}\right]$$

This can be simply done by substitution $\sigma_- \to \sigma_- e^{-i\omega_I t}$, $a \to ae^{-i\nu t}$. We will only apply lasers whose frequencies are near resonance, namely $\left|\omega_I - \omega_j\right| \ll \left|\omega_I + \omega_j\right|$, so we can drop the counter rotating terms with frequency $\omega_I + \omega_j$ safely. This step is called optical RWA. Further, for most practical cases we have $\eta\sqrt{\left\langle(a + a^\dagger)^2\right\rangle} \ll 1$, which is known as the Lamb-Dicke regime, we can preserve only the first order term in η_j. To a very good approximation H_{ion}^I becomes

$$H_{\text{ion}}^I \approx \sum_j \frac{\Omega_j}{2}\left[\sigma_+\left(I + i\eta_j ae^{-i\nu t} + i\eta_j a^\dagger e^{i\nu t}\right)e^{i(\omega_I-\omega_j)t}e^{-i\phi_j} + \text{h.c.}\right] \tag{3.5}$$

For a single resonant driving beam $\omega = \omega_I$, we have terms rotating at frequency 0 and $\pm\nu$. The latter two can again be neglected, which is known as vibrational RWA. The resulting Hamiltonian

$$H_{\text{car}} = \frac{\Omega}{2}\left(\sigma_+ e^{-i\phi} + \sigma_- e^{i\phi}\right) \tag{3.6}$$

is called the carrier transition. The carrier transition happens between $|\!\uparrow\rangle|n\rangle$ and $|\!\downarrow\rangle|n\rangle$ with Rabi frequency Ω and does not affect the motional state. Similarly if $\omega = \omega_I - \nu$ we have

$$H_{\text{rsb}} = \frac{i\eta\Omega}{2}\left(\sigma_+ ae^{-i\phi} + \sigma_- a^\dagger e^{i\phi}\right), \tag{3.7}$$

called the (first) red sideband transition. This is exactly the JCM that we have derived in (2.4). The red sideband transition happens between a Jaynes-Cumming doublet $|n\rangle|\downarrow\rangle$ and $|n-1\rangle|\uparrow\rangle$, which we already knew since the JCM conserves excitation number. Its Rabi frequency is given by

$$\Omega_{n,n-1} = \sqrt{n}\eta\Omega.$$

Starting from $|n\rangle|\downarrow\rangle$, after a π-pulse of red sideband cooling the phonon number is removed by 1. Combine this process with optical pumping we can realize the resolved sideband cooling (Fig. 3.3a). Finally, we also have the (first) blue sideband transition at $\omega = \omega_I + \nu$.

$$H_{\text{bsb}} = \frac{\mathrm{i}\eta\Omega}{2}\left(\sigma_+ a^\dagger \mathrm{e}^{-\mathrm{i}\phi} + \sigma_- a\mathrm{e}^{\mathrm{i}\phi}\right) \tag{3.8}$$

This Hamiltonian is sometimes called anti-JCM. It happens between $|n\rangle|\downarrow\rangle$ and $|n+1\rangle|\uparrow\rangle$ with Rabi frequency

$$\Omega_{n,n+1} = \sqrt{n+1}\eta\Omega.$$

While an anti-JCM cannot be realized with a direct photon-atom coupling because it violates energy conservation, here we made it successfully because the driving beam is serving extra energy.

The three kinds of transitions mentioned above are of crucial importance in experiments. The carrier transition performs single qubit rotations. A carrier π-pulse induces full population inversion between $|\downarrow\rangle$ and $|\uparrow\rangle$; a $\pi/2$-pulse makes equally-superposed states from qubit eigenstates. The sideband transitions couple ion's motional state to its internal state, which allows information stored in one ion qubit to shuttle to the others by the bus mode. There are also higher order sideband transitions, but the coupling strength is much weaker than first order ones.

3.2.3 Trapped-Ion realization of the QRM

While it is easy to realize the JCM with a single red sideband laser, it is not straightforward to simulate a genuine QRM in USC or DSC regime. Consider a red and a blue sideband transition, both detuned, as interacting terms of the trapped-ion Hamiltonian (Fig. 3.3b). Suppose detunings are small enough to perform the vibrational RWA, namely

$$\omega_{\text{r,b}} = \omega_I \mp \nu + \delta_{\text{r,b}}, \quad |\delta_{\text{r,b}}| \ll \nu.$$
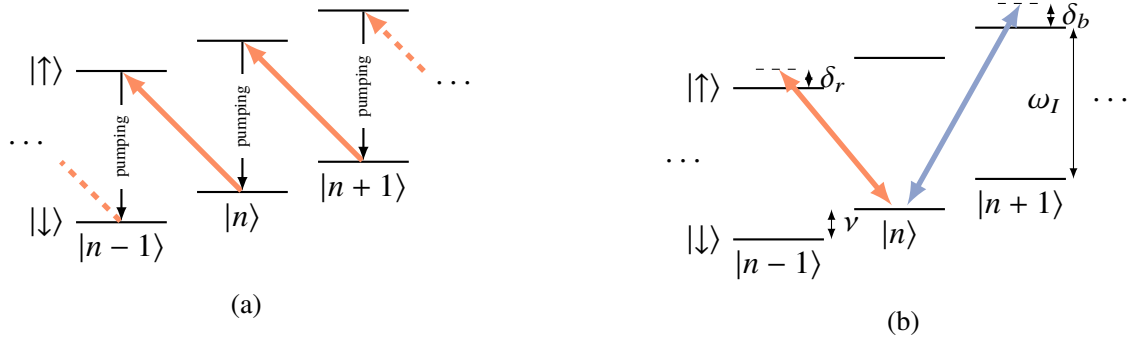
图 3.3   (a) Resolved sideband cooling. The red arrows show a red sideband π-pulse, which remove one phonon number; the black arrows show optical pumping pulse, which flip the spin back. (b) Driving beams used in the effective QRM. The red and blue arrows show a red and a blue sideband transition detuned by $\delta_{r,b} \ll \nu$ respectively. Energy levels shown are not to scale.

Take $\Omega_r = \Omega_b = \Omega_R$, $\eta_r = \eta_b = \eta$, $\phi_r = \phi_b = 3\pi/2$, by (3.5) we have

$$H^I = \frac{\eta\Omega_R}{2}\sigma_+\left(a\mathrm{e}^{-\mathrm{i}\delta_r t} + a^\dagger\mathrm{e}^{-\mathrm{i}\delta_b t}\right) + \mathrm{h.c.}$$

Move into the interaction picture of $H_\mathrm{t} = \frac{1}{2}(\delta_b - \delta_r)a^\dagger a + \frac{1}{4}(\delta_b + \delta_r)\sigma_z$, we have exactly the QRM Hamiltonian [19, 20]

$$H_\mathrm{QRM} = \omega_0 a^\dagger a + \frac{\Omega}{2}\sigma_z - \lambda\sigma_x\left(a + a^\dagger\right)$$

with effective parameters

$$\omega_0 = \frac{\delta_b - \delta_r}{2}, \quad \Omega = \frac{\delta_b + \delta_r}{2}, \quad \lambda = \frac{\eta\Omega_R}{2}. \tag{3.9}$$

Notice that H_t commutes with both $a^\dagger a$ and σ_z, so their expectation values are not affected by the interaction picture transformation. We can measure them conveniently in the lab frame. By proper choice of $\delta_{b,r}$ and Ω_R, we can in principle simulate the QRM in any regimes. Yet we still need to ensure that the Lamb-Dicke approximation is still valid when $\langle a^\dagger a \rangle$ is large.

3.3   Barium Ion: the Heat Bath

As we stated earlier, for $^{138}\mathrm{Ba}^+$ ion we can also perform a full set of quantum operations: Doppler and sideband cooling, optical pumping, single qubit rotation, detection of internal state, etc. Nevertheless, in the DPT experiment we simply employ the Ba$^+$ion as a heat bath. During an evolution we keep cooling it using electromagnetically induced transparency (EIT).

图 3.4 (a) Schematic representation of an open QRM realized by two ions. The red and blue arrow represent the detuned red and blue sideband laser respectively. The green arrow represent the lasers used in EIT cooling. The gray parabola schematically represents the trapping potential. (b) Energy levels of the Ba$^+$ion that is related to the EIT cooling. Energy levels shown are not-to-scale.

Because two ions share motional modes, even without explicit involvement of a cooling laser, the Yb$^+$ion gets cooled down simultaneously. This process is called sympathetic cooling and it is an advantage of the hybrid trap. In our DPT experiment, we use the breathing mode along axial direction of the linear trap as the quantized bosonic field, so a always designates the annihilation operator of the axial breathing mode from now on.

3.3.1 EIT Cooling

Laser cooling with electromegnetically induced transparency, usually known as EIT cooling, is an alternative sub-Doppler cooling scheme besides resolved sideband cooling [21, 22]. It utilizes two lasers coupling two ground states to a single excited states. Both lasers are set above resonance to the same detuning Δ. One is coupling laser and the other is cooling laser. Adjust the intensity of the coupling laser so that the excited states gets shifted by trap frequency. This fulfills the EIT condition so that the carrier transition is suppressed. There is a maximum absorption probability at the frequency of the red sideband transition $|n\rangle \to |n-1\rangle$, while the blue sideband transition probability is kept small. The asymmetry in sideband transition begets an overall cooling effect. For the Ba$^+$ion we use the S$_{1/2}$ and P$_{1/2}$ Zeeman substates (Fig. 3.4b). The configuration is exactly the same as Doppler cooling, bringing about experimental convenience.

3.3.2 Detection of Motional-State Populations

As we have mentioned, the fluorescent technique is applied to detect ion's spin state. To measure the expectation value of phonon number $\langle n \rangle$, we map the information of motional

state to the internal state of the ion with sideband excitation. Pump the internal state to $|\downarrow\rangle$ and suppose the motional state is $\sum_n c_n |n\rangle$, the initial state of the ion is thus

$$|\Psi(0)\rangle = |\downarrow\rangle \sum_{n=0}^{\infty} c_n |n\rangle .$$

Drive the 1st blue sideband excitation by duration t, the probability that the ion is in the excited state $|\uparrow\rangle$ is given by

$$p_\uparrow^{\text{bsb}}(t) = \sum_{n=0}^{\infty} P_n \frac{1 - \cos(\Omega_{n,n+1}t)}{2}, \tag{3.10}$$

where $P_n = |c_n|^2$. This is evidently the sum of $\frac{1}{2}\left(1 - \cos \Omega_{n,n+1}t\right)$ for each component $|\downarrow\rangle |n\rangle$. Similarly, we have for the 1st red sideband excitation

$$p_\uparrow^{\text{rsb}}(t) = \sum_{n=1}^{\infty} P_n \frac{1 - \cos(\Omega_{n-1,n}t)}{2} = \sum_{n=0}^{\infty} P_{n+1} \frac{1 - \cos(\Omega_{n,n+1}t)}{2}. \tag{3.11}$$

Notice that there is no red sideband excitation for the ground state $|\downarrow\rangle |0\rangle$, so the summation begin with $n = 1$.

Equation (3.10) and (3.11) suggest a mathematically direct way to determined P_n – measure the excited population at a series of time t, and perform Fourier transform to obtain the coefficients P_n. Especially, a perfect sine curve of $p_\uparrow^{\text{bsb}}$ suggests that the ion is cooled down to the ground state $|\downarrow\rangle |0\rangle$ pretty well.

3.3.3   Determination of Cooling Rate

It is necessary to determine κ before performing the DPT experiment, upon which the critical point g_c is dependent. Luckily there is a pretty simple way to measure the average phonon number during the cooling process by driving sideband excitation.[17, 23]

Assume that the motional states after cooling is still a thermal ensemble, then we should have a population distribution like

$$P_n = \frac{\bar{n}^n}{(1 + \bar{n})^{n+1}}, \tag{3.12}$$

where $\bar{n}$ is the ensemble average of phonon number for the thermal ensemble (See A.1). This indicates

$$\frac{P_{n+1}}{P_n} = \frac{\bar{n}}{\bar{n} + 1}$$

$$(a) \qquad\qquad\qquad (b)$$
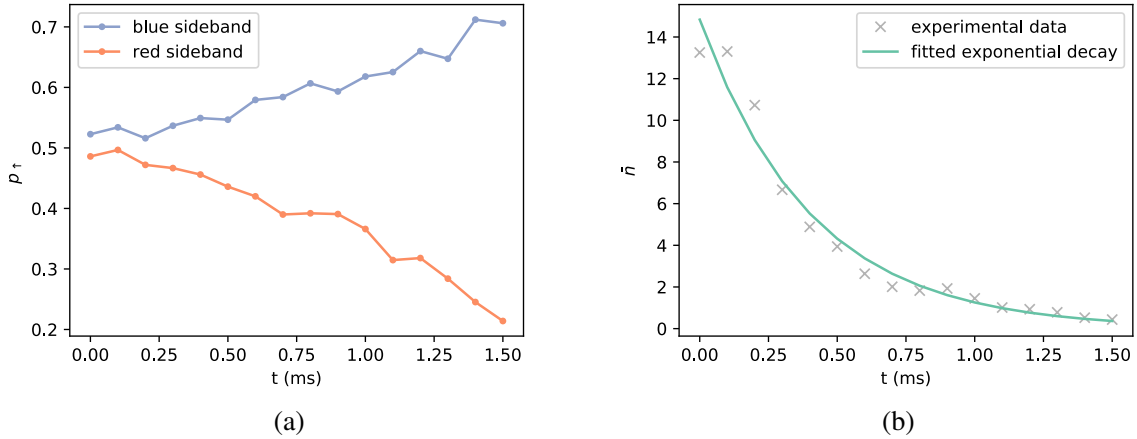
图 3.5 Measurement of the EIT cooling rate of the Ba ion, with a Yb ion also in the hybrid trap. (a) shows the population of spin-up ion during the cooling process. We can observe after sufficient cooling time the red sideband transition is suppressed, while the blue is strengthened. (b) shows the average $\bar{n}$ using (3.13). An exponential decay is fitted using the experimental data: $\bar{n} = 14.8 \exp(-2.47t)$.

is a constant. Take the ratio of equation (3.11) and (3.10), then

$$R = \frac{p_\uparrow^{\mathrm{rsb}}(t)}{p_\uparrow^{\mathrm{bsb}}(t)} = \frac{\bar{n}}{\bar{n}+1}.$$

Accordingly what we need to do is drive a red and a blue sideband excitation of equal duration and equal intensity after cooling for a certain time, detect the spin state, take the ratio, and then calculate $\bar{n}$ using

$$\bar{n} = \frac{R}{1-R}. \tag{3.13}$$

Here we show the testing result of EIT cooling of a Ba$^+$ion when a Yb$^+$ion is cooled sympathetically, namely cooling of the shared axial breathing mode. The Ba$^+$ion is initialized as $|0\rangle |\uparrow\rangle$. Turn off the cooling laser and shortly the ion gets heated again and becomes a thermal ensemble. Note that in (3.13) $\bar{n}$ is independent of the pulse duration t of sideband driving laser, because the oscillation cosine terms in (3.10) and (3.11) already cancel each other, so we only need to choose a fixed time for both processes. For the sake of reducing errors we prefer a large $p_\uparrow$ on both the numerator and the denominator, so we chose t to be the π-pulse of the blue sideband transition. The result is shown in Fig. 3.5, in which we fitted an exponential decay for $\bar{n}$

$$\bar{n} = 14.8 \times \exp(-2.47t)$$

for t in ms. Compare this with simulation results, we have

$$\kappa = 0.195 \, \text{kHz}. \tag{3.14}$$

Suppose we have $w_0 = 1 \, \text{kHz}$ for the boson field, then $\kappa = 0.195\omega_0$. This κ value already corresponds to the maximum power of the cooling laser. However, it is not a fulfilling value because the cooling rate is rather small, which can only bring about a small shift of g_c from 1 to around 1.0189. Such a tiny shift is hard to observe in experiments, which will be examined in the next section.

3.4   Experiment Scheme

The experimental realization of the QRM with trapped ions has been done since the birth of the theoretical proposal described in Sec. 3.2.3. The DSC regime of the QRM has been explored by our group members earlier [24], in which they adiabatically generated the ground states of QRM and observed the breakdown of RWA for a large coupling. Recently Cai et al. [25] has obtained strong evidence of the QPT in the QRM from some qualitative behavior of spin and bosonic observables.

The goal of my graduation project is to scrutinize the possibility to realize an open QRM in our two-species ion trap and to look for evidence of the DPT. Although I did not manage to perform an actual experiment, I would like to present some of my thoughts pertaining to experimental realization. Compared with a QPT, it is no doubt more challenging to observe a DPT. The critical point g_c is no longer fixed but modulated by the cooling parameter κ, which means g_c per se is an experimentally determined value and suffers from errors. Also, it is more time-consuming to perform numerical simulation once the dissipative term is added. The DPT does offered some convenience, though. For a DPT we are concerned with steady states in place of ground states, which are independent form the initial state. We can in principle initialize an ion to $|0\rangle |\downarrow\rangle$ normally and turn on all ad rem lasers, rather than adiabatically prepare a specified initial state.

We would like to determine the values of all effective parameters. Our experimental setup will lay constraint on parameter ranges, and we also need to fulfill the condition of all the approximations. For trapped-ion related parameters, $\omega_I \approx 2\pi \times 12.96 \, \text{GHz}$ is fixed. ν is typically $2\pi \times 1.8 \, \text{MHz}$ for our linear trap, which can be tuned within $1 \, \text{MHz}$–$3 \, \text{MHz}$. We have an η of typical value 0.122. The maximum (carrier) Rabi frequency $\Omega_R \approx 2\pi \times 100 \, \text{kHz}$ is
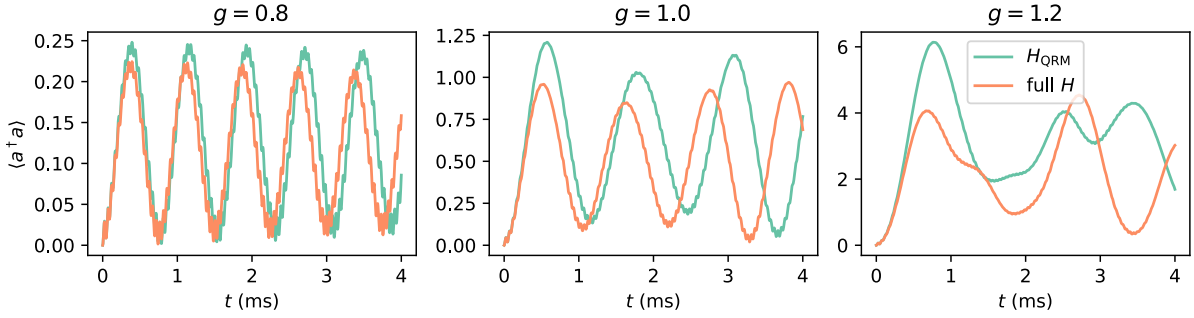
图 3.6　Deviation of full trapped ion Hamiltonian from H_{QRM} for different coupling g without dissipation. The result for Hamiltonian with Lamb-Dicke expansion to the first order coincide completely with that for H_{QRM} and it is not shown in the plot. The critical point is $g_c = 1$.

limited by the power of the 355 nm Raman laser, giving an upper bound of the coupling strength λ. For effective frequencies ω_0 and Ω in (3.9), they are related to the sum and difference of detunings and generally can vary within a broad range. Yet we must guarantee $\delta_{r,b} \ll \nu$ so that the vibrational RWA can be assumed safely. κ measured as in (3.14) is already the maximum, corresponding to the maximum power of the EIT cooling beams.

With the consideration above we pick up a set of parameters

$$\omega_0 = 2\pi \times 1\,\mathrm{kHz}, \quad \Omega = 20\omega_0, \quad g \sim 1.$$

To precisely capture the behavior of the ion simulator, we performed simulations based on the full Hamiltonian of a trapped-ion (3.4) with only optical RWA (H_{RWA} here after), and compared the results with that of the Hamiltonian after Lambe-Dicke expansion (3.5) and the effective QRM Hamiltonian (2.3). It is reasonable to perform the optical RWA here. Since our detunings are comparable to ν, which is much smaller than ω_I, the approximation condition can always get satisfied. Technically our computation speed is limited by the largest frequency involved: with a huge number it needs smaller step lengths to solve a differential equation. The optical RWA reduce the largest frequency from $\sim \omega_I$ to $\sim \nu$, which is 10^4 times smaller.

In Fig. 3.6 and Fig. 3.7 we show the non-dissipative and dissipative cases for g below, close to, and above the critical point g_c respectively. As simulation of the full ion Hamiltonian is a heavy computational task and in experiments we will restrict ourselves to small phonon numbers, the Fock space is truncated at $N = 20$ in our simulation unless mentioned otherwise.

Evident deviation of the ion Hamiltonian from the ideal QRM Hamiltonian can be observed in all the cases. Specifically, a stronger coupling brings about a larger deviation. We have also tested the Hamiltonian after Lamb-Dicke expansion, whose expectation value $\langle a^\dagger a \rangle$
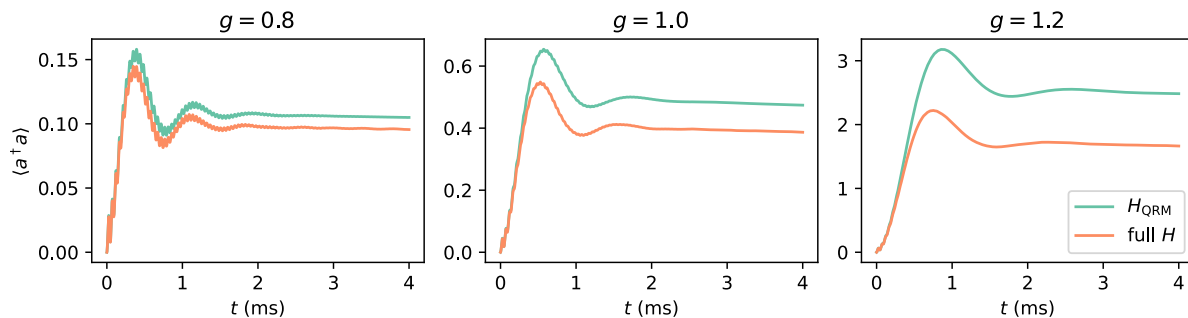
图 3.7   Deviation of full trapped ion Hamiltonian from H_{QRM} for different coupling g with the dissipation $\kappa = 0.195\omega_0$. The result for Hamiltonian with Lamb-Dicke expansion to the first order coincide completely with that for H_{QRM} and it is not shown in the plot. The critical point is $g_c = 1.02$.
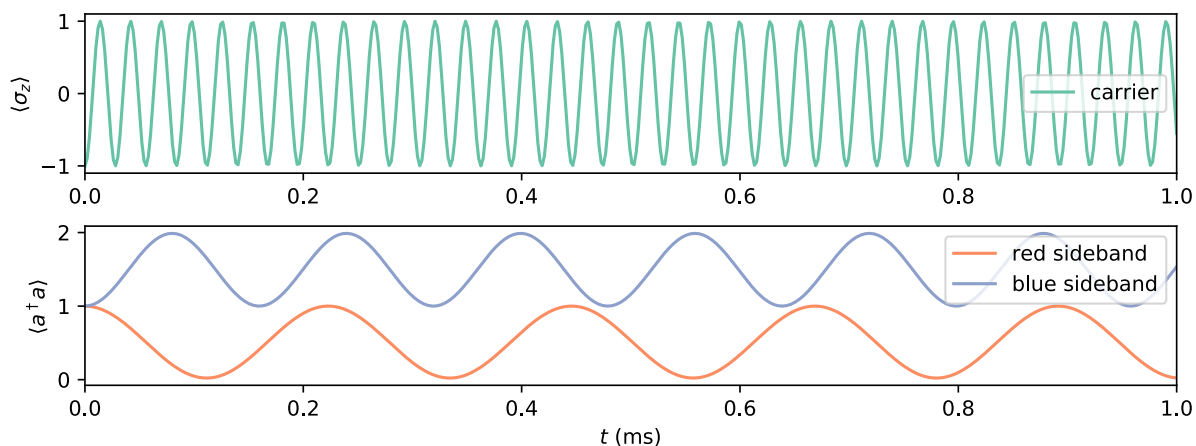
图 3.8   Carrier, red sideband, and blue sideband transition at the carrier Rabi frequency $\Omega = 36.657\,\mathrm{kHz}$ given by the full ion Hamiltonian. The simulation starts from the state $|1\rangle\,|\!\downarrow\rangle$.

turns out to completely coincide with H_{QRM}. This leads to the conclusion: the Lamb-Dicke expansion is not good in the context of our system.

It seems that the effective QRM Hamiltonian is more susceptible to the higher order expansion terms than simple coherent manipulation on the ion. Using the same parameter, carrier, red sideband, and blue sideband transition are not deteriorated by the Lamb-Dicke expansion. In Fig. 3.8 we discover both spin and phonon observables experience perfect oscillation at the expected Rabi frequency

$$\Omega = 36.66\,\mathrm{kHz}, \quad \Omega_{1,0} = 4.47\,\mathrm{kHz}, \quad \Omega_{1,2} = 6.32\,\mathrm{kHz},$$

respectively.

Despite the apparent deviation, in the dissipative case two curves show similar fluctuation trends. For this reason we can rely on the simpler QRM Hamiltonian, which consumes much
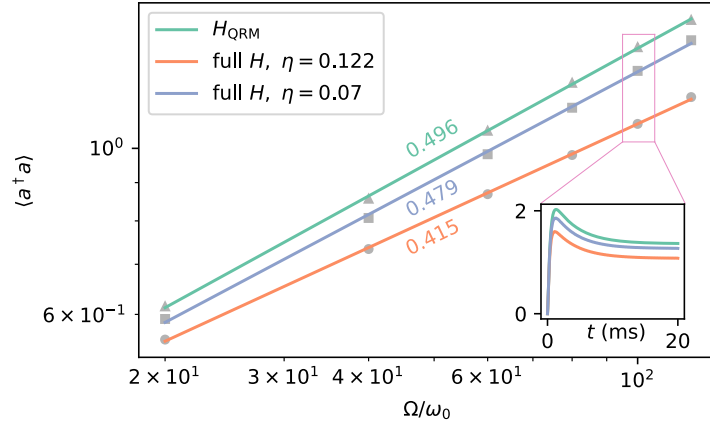
图 3.9 Finite-frequency relations of $\langle a^\dagger a \rangle$. A comparison is made between H_{QRM} and the full ion Hamiltonian at $\eta = 0.122, 0.07$. Fitted scaling exponents are shown in the figure. A dissipative term of $\kappa = 1.5\omega_0$ is taken in simulation. The inset demonstrates time evolution of $\langle a^\dagger a \rangle$ at $\Omega/\omega_0 = 100$, a relaxation time of ~ 20 ms can be discovered.

less computation power, to estimate relaxation time to reach steady state. We try to investigate the FFS properties of the ion simulator, as in Sec. 2.3. The scaling relation with respect to Ω/ω_0 is shown in Fig. 3.9. In the simulation we have taken an extremely large $\kappa = 1.5\omega_0$ in order to accelerate relaxation and hence to save calculation time (See the inset of Fig. 3.9). For this κ value it exacts around 20 ms for the slowest one to reach the steady state, and it already takes 2.5 hours to finish computation. Meanwhile, A smaller κ will not affect the result qualitatively. Obviously the exponent given by the full ion Hamiltonian is no longer valid, though the scaling law itself is. In other words, the ion Hamiltonian cannot be used to approximate the QRM Hamiltonian, but itself show a scaling relationship at the QRM critical point.

We checked the FFS function of H_{RWA}, which turns out to still collapse in to a single curve (Fig. 3.10). It also deviates from that of a QRM apparently, as plotted in the inset. Therefore, we conclude that a DPT possibly happens for a more complex model represented by H_{RWA}, but it differs from our desired QRM.

To ensure that we can work in the Lamb-Dicke regime, let's rewrite the condition as $\eta\sqrt{2\bar{n}+1} \ll 1$, where $\bar{n}$ is the average phonon number. Suppose $\eta = 0.122$ and $\bar{n} = 5$, which corresponds to $g \sim 1.3$, then $\eta\sqrt{2\bar{n}+1} \sim 0.4$ is rather large. The second order term is about 0.4 times the first order term and thus has a non-negligible influence. A smaller η value, like 0.07 [25], is then preferred. η is dependent on the effective wavevector $\mathbf{k}$ and the motional mode frequency ν. From an experimental point of view, it is difficult to change the angle between two Raman lasers to adjust $\mathbf{k}$, but ν can be controlled by the rf frequency of the trap.
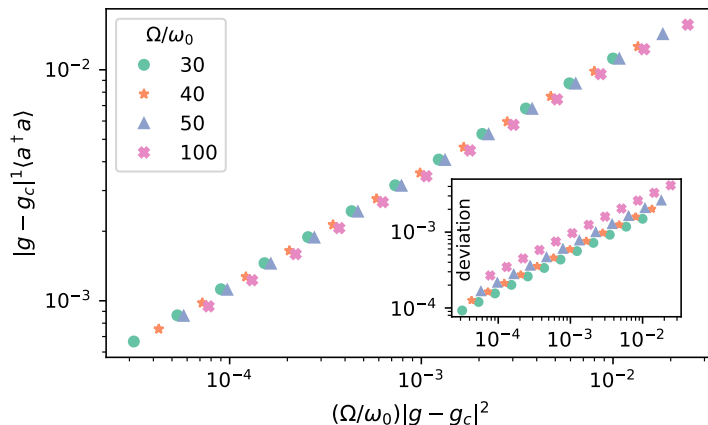
图 3.10   FFS function obtained from the full ion Hamiltonian under various frequency ratios. It can be seen that data points corresponding to different ratios still collapse into a single curve. The inset shows absolute deviation from the FFS of an ideal QRM. The relative deviation is roughly 10%.

For our system, we can have at most $\nu = 2.6\,\mathrm{MHz}$, giving $\eta = 0.102$.

The technical difficulties mentioned above hindered our plan to observe the FFS relation of the DPT. Instead of pursuing quantitative results pertaining to critical exponents, it seems more realistic to search some qualitative evidences of the DPT first, as Cai et al. [25] have done for the QPT. In Fig. 2.3 we have seen the zero to non-zero transition of n_c and $\langle \sigma_z \rangle$ as a result of breaking the Z_2 symmetry. For our DPT, the open QRM behaves in a similar way, except that the critical point gets slightly shifted (Fig. 3.11). In the simulation we have applied $\kappa = 0.195\omega_0$. For this simpler phenomenon what matters happen only near the critical point. If we choose a tender ratio like $\Omega/\omega_0 = 20$, $\langle a^\dagger a \rangle$ will stay small there, and we are not affected by higher order terms in Lamb-Dicke expansion.

We investigated the relaxation time to achieve steady state as well. Some of the time evolution results are plotted in the insets of Fig. 3.11. Typically as Ω/ω_0 increases it takes more time to reach equilibrium. For a fixed frequency ratio, it is largest near the critical point than anywhere else. We have tested $\Omega/\omega_0 =10$, 20 and 40, whose relaxation times turn out to be $10\,\mathrm{ms}$, $50\,\mathrm{ms}$ and $100\,\mathrm{ms}$ respectively, which is far beyond our typical operation duration $\sim 100\,\mathrm{s}$.

Our operation time is limited by the largest allowed duration of the single qubit rotation of Yb$^+$by stimulated Raman transition. In experiments we found that once the operation time of the Raman lasers reach $\sim 1\,\mathrm{ms}$, the Yb$^+$ion gets dark. It is yet not clear what happens; possibly the ion goes to some unknown states or becomes other ion forms.

Is it possible to shorten the required relaxation time? It may seem that we can do it by altering ω_0, which defines the time scale of the QRM. For non-dissipative case this is indeed
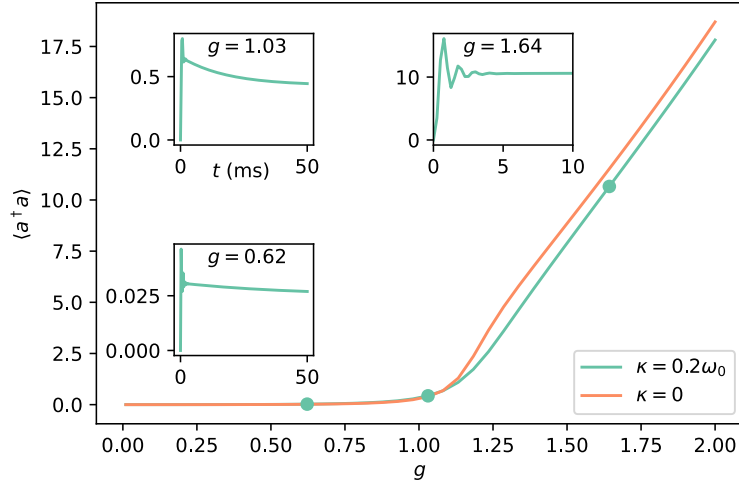
图 3.11 Phonon number expectation value near the critical point, at frequency ratio $\Omega/\omega_0 = 20$, of H_{QRM}. The result of the non-dissipative case is also drawn for comparison. A small shift of the critical point can be seen, but limited by finite frequency ratio, it is hard to say where the critical point exactly lies. The insets exhibit time evolution of three selected points, from which a relaxation time around 50 ms can be determined.

true: double ω_0 and accordingly Ω, λ, we can finish the simulation within half its original duration. The only thing we need to pay attention is that, as λ is doubled, we need a larger Rabi frequency Ω_R. However, for the DPT, the trick is not useful since the absolute value of κ cannot be enlarged beyond 0.195 kHz: if we take $\omega_0 = 2$ kHz, then we can have at most $\kappa = 0.098\omega_0$. The net effect is an almost unchanged relaxation time.

A very effective way to optimize is of course to enlarge the cooling rate, although it is not possible for our currrent system setup. A larger shift of g_c will be induced by a larger κ, showing clearly the difference between the ordinary QPT and the DPT. The range in which g_c belongs to can be observed directly form $\langle a^\dagger a \rangle$ plot. In contrast, with our current setup we can only claim there is a turning point, but cannot say it is shifted remarkably form the QPT critical point $g_c = 1$.

Chapter 4   Discussions and Conclusion

The thesis presented an experimental scheme to realize a dissipative phase transition of the quantum Rabi model in a hybrid trapped-ion system. A Yb$^+$ion is employed as the simulator and it is damped by a Ba$^+$ion through sympathetic cooling. The last section explains reasons that account for the failure of experimental realization of the DPT. An unfavorable Lambe-Dicke parameter, a weak cooling power, and a short Raman operation time form our main obstacles.

Even with these shortages fixed, our investigation suggests that it is very challenging to observe the finite-frequency scaling behavior, like that in Fig. 2.6 of the DPT as we have first proposed. Scaling relation at the critical point requires a range of Ω/ω_0, especially large values. But for a large frequency ratio, the Lamb-Dicke expansion is deteriorated because of the influence of the carrier term. If we examine the collapse property of the FFS function, it is still hard since we suffer from experimental noises like heating of the motional mode, dephasing noise of the qubit, etc. Because g actually varies within a very small range near the critical point, the data points are extremely susceptible to those noises. Generally we cannot expect the FFS functions to still collapse into a single curve with experimental noises.

In spite of the difficulties to find out quantitative results. We are still optimistic that proposals like the one presented in Fig. 3.11 is highly possible to be fulfilled. After adequate optimization it is possible to observe the zero to non-zero transition of such kinds.

Bibliography

[1] I. I. Rabi. On the process of space quantization. *Physical Review*, 49(4):324, 1936.

[2] I. I. Rabi. Space quantization in a gyrating magnetic field. *Physical Review*, 51(8):652, 1937.

[3] Edwin T Jaynes and Frederick W Cummings. Comparison of quantum and semiclassical radiation theories with application to the beam maser. *Proceedings of the IEEE*, 51(1): 89–109, 1963.

[4] Bruce W Shore and Peter L Knight. The jaynes-cummings model. *Journal of Modern Optics*, 40(7):1195–1238, 1993.

[5] Subir Sachdev. *Quantum Phase Transitions*. Cambridge University Press, 2nd edition, 2011. ISBN 0521514681,9780521514682.

[6] Christopher Gerry and Peter Knight. *Introductory quantum optics*. Cambridge University Press, 2005.

[7] Daniel Braak. Integrability of the rabi model. *Physical Review Letters*, 107(10):100401, 2011.

[8] Qing-Hu Chen, Chen Wang, Shu He, Tao Liu, and Ke-Lin Wang. Exact solvability of the quantum rabi model using bogoliubov operators. *Physical Review A*, 86(2):023822, 2012.

[9] Honghua Zhong, Qiongtao Xie, Murray T Batchelor, and Chaohong Lee. Analytical eigenstates for the quantum rabi model. *Journal of Physics A: Mathematical and Theoretical*, 46(41):415302, 2013.

[10] Myung-Joong Hwang, Ricardo Puebla, and Martin B Plenio. Quantum phase transition and universal dynamics in the rabi model. *Physical review letters*, 115(18):180404, 2015.

[11] Fa Wang. Lecture notes in advanced quantum mechanics, September 2018.

[12] Steven M Girvin and Kun Yang. *Modern condensed matter physics*. Cambridge University Press, 2019.

[13] Ricardo Puebla. *Equilibrium and Nonequilibrium Aspects of Phase Transitions in Quantum Physics*. Springer, 2018.

[14] J.G. Brankov. *Introduction to the Finite-Size Scaling*. Leuven University Press, 1996. ISBN 9061867584,9789061867586.

[15] Myung-Joong Hwang, Peter Rabl, and Martin B Plenio. Dissipative phase transition in the open quantum rabi model. *Physical Review A*, 97(1):013825, 2018.

[16] John Preskill. Lecture notes for ph219/cs219: Quantum information, 2018. URL: `http://theory.caltech.edu/~preskill/ph219/index.html#lecture`. Last visited on 2021/05/22.

[17] Dietrich Leibfried, Rainer Blatt, Christopher Monroe, and David Wineland. Quantum dynamics of single trapped ions. *Reviews of Modern Physics*, 75(1):281, 2003.

[18] Dingshun Lü. *Experimental study of quantum optics in a trapped ion system*. PhD thesis, Tsinghua University, 2018.

[19] JS Pedernales, I Lizuain, S Felicetti, G Romero, L Lamata, and E Solano. Quantum rabi model with trapped ions. *Scientific reports*, 5(1):1–7, 2015.

[20] Ricardo Puebla, Myung-Joong Hwang, Jorge Casanova, and Martin B Plenio. Probing the dynamics of a superradiant quantum phase transition with a single trapped ion. *Physical review letters*, 118(7):073001, 2017.

[21] Giovanna Morigi, Jürgen Eschner, and Christoph H Keitel. Ground state laser cooling using electromagnetically induced transparency. *Physical review letters*, 85(21):4458, 2000.

[22] CF Roos, D Leibfried, A Mundt, F Schmidt-Kaler, J Eschner, and R Blatt. Experimental demonstration of ground state laser cooling with electromagnetically induced transparency. *Physical review letters*, 85(26):5547, 2000.

[23] Simon Webster. *Raman sideband cooling and coherent manipulation of trapped ions*. PhD thesis, University of Oxford, 2005.

[24] Dingshun Lv, Shuoming An, Zhenyu Liu, Jing-Ning Zhang, Julen S Pedernales, Lucas Lamata, Enrique Solano, and Kihwan Kim. Quantum simulation of the quantum rabi model in a trapped ion. *Physical Review X*, 8(2):021027, 2018.

[25] M-L Cai, Z-D Liu, W-D Zhao, Y-K Wu, Q-X Mei, Y Jiang, L He, X Zhang, Z-C Zhou, and L-M Duan. Observation of a quantum phase transition in the quantum rabi model with a single trapped ion. *Nature communications*, 12(1):1–8, 2021.

[26] J Robert Johansson, Paul D Nation, and Franco Nori. Qutip: An open-source python framework for the dynamics of open quantum systems. *Computer Physics Communications*, 183(8):1760–1772, 2012.

Appendix A   Quantum Optics

A.1   Thermal Fields

Consider a single-mode field in thermal equilibrium with temperature T. Its density matrix can be computed directly using canonical ensemble.

$$\rho = \frac{e^{-\beta H}}{Z}, \quad Z = \text{tr}\left[e^{-\beta H}\right]$$

where $\beta = 1/(k_B T)$ is the inverse of the temperature. For $H = \hbar\omega\left(n + \frac{1}{2}\right)$

$$Z = \sum_{n=0}^{\infty} \langle n|e^{-\beta H}|n\rangle = \sum_{n=0}^{\infty} e^{-\beta\hbar\omega\left(n+\frac{1}{2}\right)} = \frac{e^{-\beta\hbar\omega/2}}{1 - e^{-\beta\hbar\omega}}.$$

And the diagonal elements of the density matrix, which is the population of n-photon component, is given by

$$P_n = \langle n|\rho_{\text{th}}|n\rangle = \frac{1}{Z}e^{-\beta\hbar\omega\left(n+\frac{1}{2}\right)}$$

The ensemble average of the phonon number $\bar{n}$ is thus given by

$$\bar{n} = \text{tr}[n\rho_{\text{th}}] = \frac{1}{Z}\sum_{n=0}^{\infty} n e^{-\beta\hbar\omega\left(n+\frac{1}{2}\right)} = \left(1 - e^{-\beta\hbar\omega}\right)\left(-\frac{1}{\hbar\omega}\right)\frac{d}{d\beta}\sum_{n=0}^{\infty} e^{-\beta\hbar\omega n} = \frac{1}{e^{\beta\hbar\omega} - 1}.$$

With this we can express $e^{-\beta\hbar\omega}$ as well as the probability P_n by average phonon number $\bar{n}$ as follows:

$$\rho_{\text{th}} = \frac{1}{1 + \bar{n}}\sum_{n=0}^{\infty}\left(\frac{\bar{n}}{\bar{n} + 1}\right)^n |n\rangle\langle n|, \tag{A.1}$$

$$P_n = \frac{\bar{n}^n}{(1 + \bar{n})^{n+1}}. \tag{A.2}$$

A.2   Bogoliubov Transformation

For a pair of boson annihilation and creation operators $b, b^\dagger$, we have the canonical commutation relation $\left[b, b^\dagger\right] = 1$. Make a linear combination of them and define a new pair

of operators

$$a = ub + vb^\dagger,$$
$$a^\dagger = v^* b + u^* b^\dagger.$$

Because

$$\left[a, a^\dagger\right] = \left[ub + vb^\dagger, v^* b + u^* b^\dagger\right] = |u|^2 - |v|^2,$$

under the condition $|u|^2 - |v|^2 = 1$ the canonical commutation relation is preserved by the transformation. This transformation is similar to a unitary transformation $\begin{bmatrix} u & v \\ -v^* & u* \end{bmatrix}$ up to a minus sign. While we can parametrize a unitary transformation with sinusoidal functions, we can do for the Bogoliubov transformation with hyperbolic functions:

$$u = e^{i\theta_1} \cosh r,$$
$$v = e^{i\theta_2} \sinh r.$$

Consider for example

$$H_\mathrm{q} = c_1 a^\dagger a + c_2 \left(a + a^\dagger\right)^2 + c_0. \tag{A.3}$$

We have

$$
\begin{aligned}
H_\mathrm{q} &= c_1 \left(v^* b + u^* b^\dagger\right)\left(ub + vb^\dagger\right) + c_2\left(ub + vb^\dagger + v^* b + u^* b^\dagger\right)^2 + c_0 \\
&= \left[(c_1 + 2c_2)\left(|u|^2 + |v|^2\right) + 2c_2(uv + u^* v^*)\right] b^\dagger b \\
&\quad + \left[c_1 u^* v + c_2(v + u^*)^2\right]\left(b^\dagger\right)^2 \\
&\quad + \left[c_1 v^* u + c_2(u + v*)^2\right] b^2 \\
&\quad + \left[c_0 + c_1 |v|^2 + c_2(u + v^*)(v + u^*)\right].
\end{aligned}
$$

By setting $c_1 u^* v + c_2(v + u^*)^2 = 0$ we can clear the off-diagonal terms. Take $\theta_1 = \theta_2 = 0$:

$$c_1 \cosh r \sinh r + c_2(\cosh r + \sinh r)^2 = 0,$$

$$\frac{c_1}{2} \sinh 2r + c_2(\cosh 2r + \sinh 2r) = 0,$$

$$r = -\frac{1}{4} \ln\left(\frac{4c_2}{c_1} + 1\right).$$

By the way,

$$H_q = [(c_1 + 2c_2)\cosh 2r + 2c_2 \sinh 2r]b^\dagger b + c(g),$$

with $c(g)$ a constant term dependent on g.

For the normal phase Hamiltonian H_{np} in (2.6), $c_1 = \omega_0, c_2 = -\omega_0 g^2/4, c_0 = -\Omega/2$, thus

$$r_{\mathrm{np}} = -\frac{1}{4}\ln(1 - g^2),$$

$$H_{np} = \omega_0\sqrt{1 - g^2}\,a^\dagger a + E_{\mathrm{G,np}}(g)$$

The Bogoliubov transformation can also be represented by a squeeze operator

$$\mathcal{S}(\xi) = \exp\left[\frac{1}{2}(\xi a^2 - \xi a^{\dagger 2})\right],$$

where $\xi = re^{i\theta}$ is a complex number. From the commutation relations

$$\left[\frac{1}{2}(\xi a^{\dagger 2} - \xi^* a^2), a\right] = -\xi a^\dagger, \quad \left[\frac{1}{2}(\xi a^{\dagger 2} - \xi^* a^2), a^\dagger\right] = -\xi^* a$$

and Baker-Hausdorff formula, it follows that

$$
\begin{aligned}
\mathcal{S}^\dagger(\xi) a \mathcal{S}(\xi) &= a - \xi a^\dagger + \frac{1}{2!}|\xi|^2 a - \frac{1}{3!}|\xi|^2 \xi a^\dagger + \dots \\
&= a\sum_{n=0}^{\infty}\frac{1}{(2n)!}|\xi|^{2n} - \xi a^\dagger \sum_{n=0}^{\infty}\frac{1}{(2n+1)!}|\xi|^{2n} \\
&= a\sum_{n=0}^{\infty}\frac{r^{2n}}{(2n)!} - e^{i\theta}a^\dagger \sum_{n=0}^{\infty}\frac{r^{2n+1}}{(2n+1)!} \\
&= a\cosh r - a^\dagger e^{i\theta}\sinh r.
\end{aligned}
\tag{A.4}
$$

and thus

$$\mathcal{S}^\dagger(\xi) a^\dagger \mathcal{S}(\xi) = a^\dagger \cosh r - a e^{-i\theta}\sinh r. \tag{A.5}$$

With the identification $\theta = \pi$ our desired transformation can be performed by (A.4) and (A.5) with $\mathcal{S}(-r)$. So if the eigenstates in the transformed Fock basis are $|n\rangle$, then before transformation we have in the tensor product space

$$\left|\psi_{\mathrm{np}}^n\right\rangle = \mathcal{S}\left(-r_{\mathrm{np}}\right)|n\rangle\,|\!\downarrow\rangle.$$

A.3 Superradiant Phase Effective Hamiltonian

In quantum optics, the displacement operator $\mathcal{D}(\alpha)$ is defined as

$$\mathcal{D}(\alpha) = \exp(\alpha a^{\dagger} - \alpha^* a),$$

where α is a complex number. It generates a displacement in phase space, using operator formalism that is

$$\mathcal{D}^{\dagger}(\alpha) a \mathcal{D}(\alpha) = a + \alpha. \tag{A.6}$$

Therefore, a transformation on H_{QRM} gives rise to

$$\mathcal{D}^{\dagger}(\alpha) H_{\text{QRM}} \mathcal{D}(\alpha) = \omega_0 (a^{\dagger} + \alpha)(a + \alpha) + \frac{\Omega}{2}\sigma_z - \lambda(a + a^{\dagger})\sigma_x - 2\lambda\alpha\sigma_x.$$

Then we transform the spin part by [13]

$$U = \begin{bmatrix} \cos\theta & -\sin\theta \\ \sin\theta & \cos\theta \end{bmatrix}$$

with respect to the basis $|\uparrow\rangle = \begin{bmatrix} 1 \\ 0 \end{bmatrix}, |\downarrow\rangle = \begin{bmatrix} 0 \\ 1 \end{bmatrix}$ so that $|\Uparrow\rangle = U|\uparrow\rangle, |\Downarrow\rangle = U|\downarrow\rangle$. Denote the Pauli matrices with respect to the new basis by $\tau_{x,y,z}$, the previous Pauli matrices are transformed into

$$U^{\dagger}\sigma_z U = \begin{bmatrix} \cos 2\theta & -\sin 2\theta \\ -\sin 2\theta & -\cos 2\theta \end{bmatrix} = \cos 2\theta \tau_z - \sin 2\theta \tau_x,$$

$$U^{\dagger}\sigma_x U = \begin{bmatrix} \sin 2\theta & \cos 2\theta \\ \cos 2\theta & -\sin 2\theta \end{bmatrix} = \sin 2\theta \tau_z + \cos 2\theta \tau_x.$$

So in respect of the new basis

$$\mathcal{D}^{\dagger}(\alpha) H_{\text{QRM}} \mathcal{D}(\alpha) = w_0 a^{\dagger} a + \omega_0 \alpha^2 + (\omega_0 \alpha - \lambda \sin 2\theta \tau_z)(a + a^{\dagger}) - \lambda \cos 2\theta (a + a^{\dagger})\tau_x$$
$$+ \left(\frac{\Omega}{2}\cos 2\theta - 2\lambda\alpha \sin 2\theta\right)\tau_z - \left(\frac{\Omega}{2}\sin 2\theta + 2\lambda\alpha \cos 2\theta\right)\tau_x.$$

Choose θ such that $\tan 2\theta = -4\lambda\alpha/\Omega$, then

$$\mathcal{D}^\dagger(\alpha)H_{\text{QRM}}\mathcal{D}(\alpha) = w_0 a^\dagger a + \omega_0\alpha^2 + (\omega_0\alpha - \lambda\sin 2\theta\,\tau_z)(a + a^\dagger) - \lambda\cos 2\theta(a + a^\dagger)\tau_x + \frac{\Omega}{2}\frac{1}{\cos 2\theta}\tau_z.$$

Denote $\Omega/\cos 2\theta$ as $\tilde{\Omega} = \sqrt{\Omega^2 + 16\lambda^2\alpha^2}$, and choose α so that $\omega_0\alpha + \lambda\sin 2\theta = 0$, the solution is given by $\pm\alpha_g$ and

$$\alpha_g = \sqrt{\frac{\Omega(g^4 - 1)}{4g^2\omega_0}}, \quad g = \frac{2\lambda}{\sqrt{\Omega\omega_0}}.$$

In this case, we can further simplify the Hamiltonian

$$\mathcal{D}^\dagger(\pm\alpha_g)H_{\text{QRM}}\mathcal{D}(\pm\alpha_g) = w_0 a^\dagger a + \frac{\tilde{\Omega}}{2}\tau_z + \omega_0\alpha^2 - \lambda\cos 2\theta(a + a^\dagger)\tau_x \pm 2\omega_0\alpha_g\,|\Uparrow\rangle\langle\Uparrow|\,(a + a^\dagger).$$

In the limit of $\Omega/\omega_0 \to \infty$ and fixed g, the last term which is of order $(\Omega/\omega_0)^{1/2}$ and hence can be neglected. So the Hamiltonian goes back to the form of H_{QRM} with effective parameters

$$\tilde{\Omega} = \sqrt{\Omega^2 + 16\lambda^2\alpha_g^2} = g^2\Omega, \quad \tilde{\lambda} = \lambda\cos 2\theta = \frac{\sqrt{\omega_0\Omega}}{2g}.$$

That is

$$\tilde{H}_{\text{QRM}}(\pm\alpha_g) = \omega_0 a^\dagger a + \frac{\tilde{\Omega}}{2}\tau_z - \tilde{\lambda}(a + a^\dagger)\tau_x + \omega_0\alpha_g^2.$$

Conduct a unitary transformation to diagonalize the spin part of $\tilde{H}_{\text{QRM}}$, just as what we have done in (2.5), then project the spin part onto $|\Downarrow\rangle$, we obtain

$$H_{\text{sp}} = \langle\Downarrow|H'|\Downarrow\rangle = \omega_0 a^\dagger a - \frac{\omega_0}{4g^4}(a + a^\dagger)^2 - \frac{\Omega}{4}(g^2 + g^{-2}).$$

Finally, we perform a Bogoliubov transformation with identification that $c_1 = \omega_0$, $c_2 = -\omega_0/(4g^4)$ and $c_0 = -\Omega(g^2 + g^{-2})/4$ in (A.3).

$$r_{\text{sp}} = -\frac{1}{4}\ln\left(1 - \frac{1}{g^4}\right),$$

$$H_{\text{sp}} = \omega_0\sqrt{1 - \frac{1}{g^4}}\,a^\dagger a + E_{\text{G,sp}}(g).$$

And we can identify the eigenstates

$$\left|\psi_{\text{sp}}^n\right\rangle = \mathcal{D}(\pm\alpha_g)\mathcal{S}(-r_{\text{sp}})\,|n\rangle\,|\downarrow^\pm\rangle,$$

with $|\!\downarrow^{\pm}\rangle$ denoting the transformed spin basis corresponding to $\pm\alpha_g$ respectively.

$$|\!\downarrow^{\pm}\rangle = \mp\sqrt{\frac{1-g^{-2}}{2}}\,|\!\uparrow\rangle + \sqrt{\frac{1+g^{-2}}{2}}\,|\!\downarrow\rangle .$$

Appendix B   Source Code

All the scripts are programmed using python, and our customary environment is python 3.6. The simulations are largely based on the Quantum Toolbox in Python (QuTiP) package [26] (version 4.6.2). The simulation of H_{RWA}, with the Lamb-Dicke expansion or not, will consume much more computation power than that of H_{QRM}, so I have take advantage of the free cluster Teaching II of Peking University to do multiprocessing. Some most important scripts are pasted and explained below.

B.1   bedrock.py

This file is a collection of commonly used objects. Each function has a docstring that describes its usage. We will frequently import functions from this file and you can use it to perform your own simulation if you are interested in our topic.

The `Laser` class, as a subclass of `namedtuple`, is merely a tuple to pack a laser's frequency, Lamb-Dicke parameter, and Rabi frequency together. Then the information of a laser is stored in a single object and can be passed into `H_RWA` conveniently. You can pass a list of `Laser` objects to `H_RWA` if you want multiple lasers to act on the ion simultaneously.

```python
import numpy as np
import matplotlib.pyplot as plt
import seaborn as sns
from collections import namedtuple
from qutip import *

Laser = namedtuple('Laser', 'freq, eta, Rabi')
omegaI = 12.64281211846 * 10 ** 9 * 2 * np.pi

def pauli_matrices(dim):
    '''
    pauli matrices in the tensor product space

    param:
        dim: dimension of the Fock space
    return:
        (sm, sx, sy, sz) as a tuple, with pauli_matrices(dim)[0] pointing to sigma_minus
    '''
    sx = tensor(sigmax(), qeye(dim))
    sy = tensor(sigmay(), qeye(dim))
    sz = tensor(sigmaz(), qeye(dim))
    sm = tensor(sigmam(), qeye(dim))
    return sm, sx, sy, sz

def destroy_a(dim):
```

```python
26          '''
27          bosonic annihilation operator in the tensor product space
28          '''
29          return tensor(qeye(2), destroy(dim))
30
31      def H_QRM(w0, W, l, dim):
32          '''
33          Quantum Rabi Model Hamiltonian
34
35          expression: 1/2 * W * sz + w0 * a.dag() * a + l * sx * (a + a.dag())
36          '''
37          _, sx, _, sz = pauli_matrices(dim)
38          a = destroy_a(dim)
39          return 1/2 * W * sz + w0 * a.dag() * a + l * sx * (a + a.dag())
40
41      def g2l(g, w0, W):
42          '''
43          transform dimensionless coupling factor g to lambda with freqency unit
44
45          param: g, w0, W
46          '''
47          return g / 2 * np.sqrt(w0 * W)
48
49      def l2g(l, w0, W):
50          '''
51          transform frequency-unit coupling factor lambda to dimensionless g
52
53          param: l, w0, W
54          '''
55          return 2 * l / np.sqrt(w0 * W)
56
57      def H_RWA(dim, omegaI, nu, lasers, LD=False):
58          '''
59          Trapped ion Hamiltonian with only optical RWA. Multiple interaction terms are applied
60          if there are more than 1 item in 'lasers' list.
61          param:
62              dim: dimension of the Fock space
63              omegaI: internal state energy gap (qubit gap)
64              nu: motional state energy gap (motional mode freq.)
65              lasers: a list of class Laser object.
66              LD: bool value, if True, then apply the first order Lamb-Dicke approximation.
67
68          return:
69              pack: time-dependent Hamiltonian defined in QuTiP
70          '''
71          sm = pauli_matrices(dim)[0]
72          a = destroy_a(dim)
73          H0 = nu * a.dag() * a
74          pack = [H0]   # store final Hamiltonian in time-dependent form
75          for laser in lasers:
76              b = 1j * laser.eta * (a + a.dag())
77              if not LD:   # default case
78                  H1 = sm.dag() * b.expm()
79                  H2 = sm * b.dag().expm()
80              else:   # LD case
81                  H1 = sm.dag() * (1 + b)
82                  H2 = sm * (1 - b)
83              c1 = f'{laser.Rabi} / 2 * exp(1j * ({omegaI} - {laser.freq}) * t)'
```

```
84        c2 = f'{laser.Rabi} / 2 * exp(-1j * ({omegaI} - {laser.freq}) * t)'
85        pack.append([H1, c1])
86        pack.append([H2, c2])
87    return pack
```

B.2   ion_scaling.py

This piece generates Fig. 3.9. While the simulation with `H_QRM` usually takes several minutes, it is time-consuming to simulate with `H_RWA`, which takes about an hour for each evolution process. We ran the time-evolution code in parallel on a server. `parallel_map` is a handy built-in function of QuTiP to run multiprocessing.

```
1   from bedrock import *
2   from numpy import pi, sqrt, log
3   sns.set_palette('Set2')
4
5   N = 20  # Fock space truncation
6   a = destroy_a(N)
7   sz = pauli_matrices(N)[3]
8
9   nu = 1e6 * 2 * pi
10  eta = 0.122
11  w0 = 1000 * (2 * np.pi) # Rabi omega_0
12  kappa = 1.5 * w0
13  gc = sqrt(1 + (kappa / w0) ** 2)
14
15
16  def func(ratio):
17      '''
18      A packed function aiming to be called in a parallel map.
19      '''
20      W = ratio * w0
21      lc = g2l(gc, w0, W)
22      f_Rabi = 2 * lc /eta
23      delta_r = W - w0
24      delta_b = w0 + W
25      init = tensor(basis(2, 1), basis(N, 0))
26
27      H1 = H_QRM(w0, W, lc, N)  # ideal QRM
28      laser1 = Laser(omegaI - nu + delta_r, eta, f_Rabi)
29      laser2 = Laser(omegaI + nu + delta_b, eta, f_Rabi)
30      H2 = H_RWA(N, omegaI, nu, [laser1, laser2])  # full ion H
31      H3 = H_RWA(N, omegaI, nu, [laser1, laser2], LD=True)  # full ion H with LD
32
33      tlist = np.linspace(0, 0.02, 1000)
34      result1 = mesolve(H1, init, tlist, [sqrt(2 * kappa) * a], [a.dag() * a])
35      result2 = mesolve(H2, init, tlist, [sqrt(2 * kappa) * a], [a.dag() * a],
36                        options=Options(nsteps=8000))
37      result3 = mesolve(H3, init, tlist, [sqrt(2 * kappa) * a], [a.dag() * a],
38                        options=Options(nsteps=8000))
39      result = [result1, result2, result3]
40
41      qsave(result, f'ratio_{ratio}')  # save result as a pickle
42      return result
```

45

```python
43
44
45  # Run on server in parallel(~1h for each)
46  ratiolist = [20, 40, 60, 80, 100, 120]
47  result = parallel_map(func, ratiolist, progress_bar=True)
48  qsave(result, 'ion_scaling_result')  # save altogether result
49  # change eta to 0.07 and repeat
50  eta = 0.07
51  re_small_eta = parallel_map(func, ratiolist, progress_bar=True)
52  qsave(result_small_eta, 'ion_scaling_result_eta0.07')
53
54
55  # Plot can be done locally
56  # If saved file is used, run the following 2 lines to load pickles.
57  # result = qload('./ion_scaling_result')
58  # re_small_eta = qload('./ion_scaling_result_eta0.07')
59
60  # curve fit
61  ffs_qrm = [re[0].expect[0][-1] for re in result]
62  ffs_ion = [re[1].expect[0][-1] for re in result]
63  ffs_small_eta = [re[1].expect[0][-1] for re in re_small_eta]
64  fit1 = np.polyfit(log(ratiolist), log(ffs_qrm), 1)
65  fit2 = np.polyfit(log(ratiolist), log(ffs_ion), 1)
66  fit3 = np.polyfit(log(ratiolist), log(ffs_small_eta), 1)
67  y1 = ratiolist ** fit1[0] * np.e ** fit1[1]
68  y2 = ratiolist ** fit2[0] * np.e ** fit2[1]
69  y3 = ratiolist ** fit3[0] * np.e ** fit3[1]
70
71  # plot
72  from mpl_toolkits.axes_grid1.inset_locator import inset_axes
73
74  fig, ax = plt.subplots(figsize=(5, 3), constrained_layout=True)
75  ax.plot(ratiolist, ffs_qrm, '^', c=sns.color_palette()[-1], markersize=4)
76  ax.plot(ratiolist, ffs_ion, 'o', c=sns.color_palette()[-1], markersize=4)
77  ax.plot(ratiolist, ffs_small_eta, 's', c=sns.color_palette()[-1], markersize=4)
78
79  ax.plot(ratiolist, y1, label=r'$H_\mathrm{QRM}$')
80  ax.plot(ratiolist, y2, label=r'full $H,\ \eta = 0.122$')
81  ax.plot(ratiolist, y3, label=r'full $H,\ \eta = 0.07$')
82
83  ax.set_xscale('log')
84  ax.set_yscale('log')
85  ax.set_xlabel(r'$\Omega/\omega_0$', fontsize=11)
86  ax.set_ylabel(r'$\langle a^\dagger a\rangle$', fontsize=11)
87  ax.legend()
88
89  ax.text(45, 0.97, f'{fit1[0]:.3}', c=sns.color_palette()[0], rotation=30)
90  ax.text(45, 0.72, f'{fit2[0]:.3}', c=sns.color_palette()[1], rotation=26)
91  ax.text(45, 0.81, f'{fit3[0]:.3}', c=sns.color_palette()[2], rotation=28)
92
93  # inset
94  inset_ax = inset_axes(ax, 1, 0.8, bbox_to_anchor=(0.96, 0.46), bbox_transform=ax.transAxes)
95  inset_ax.plot(result[4][0].times * 1000, result[4][0].expect[0])
96  inset_ax.plot(result[4][1].times * 1000, result[4][1].expect[0])
97  inset_ax.plot(re_small_eta[4][1].times * 1000, re_small_eta[4][1].expect[0])
98  inset_ax.text(6, -0.5, r'$t$ (ms)')
99
100 # inset marker
```

```
101  ax.plot([95, 106], [1.02, 1.02], linewidth=0.5, c=sns.color_palette()[3])
102  ax.plot([95, 106], [1.42, 1.42], linewidth=0.5, c=sns.color_palette()[3])
103  ax.plot([106, 106], [1.02, 1.42], linewidth=0.5, c=sns.color_palette()[3])
104  ax.plot([95, 95], [1.02, 1.42], linewidth=0.5, c=sns.color_palette()[3])
105  ax.plot([95, 72], [1.02, 0.845], linewidth=0.5, c=sns.color_palette()[3])
106  ax.plot([106, 117.5], [1.02, 0.845], linewidth=0.5, c=sns.color_palette()[3])
107
108  plt.savefig('./ion_scaling.pdf')
```

B.3   ion_ffs.py

This piece generates Fig. 3.10. Caution: this script takes around half a day to run because there are 4 ratios and lots of x values to compute.

```
1   from bedrock import *
2   from numpy import pi, sqrt, log
3   sns.set_palette('Set2')
4
5   N = 20   # Fock space truncation
6   a = destroy_a(N)
7   sz = pauli_matrices(N)[3]
8
9   nu = 1e6 * 2 * pi
10  eta = 0.122
11  w0 = 1000 * (2 * np.pi) # Rabi omega_0
12  kappa = 1.5 * w0
13  gc = sqrt(1 + (kappa / w0) ** 2)
14
15  ratiolist = [30, 40, 50, 100]
16  xlist = {ratiolist[i]:np.logspace(-4.5 + 0.13 * i, -2 + 0.13 * i, 12) for i in range(4)}
17  ylist = {30:[], 40:[], 50:[], 100:[]}  # store result
18
19
20  def func(x):
21      '''
22      A packed function aiming to be called in a parallel map.
23      '''
24      g = gc - (x / ratio) ** (1 / 2)  # x -> g -> l for substitution into H_RWA
25      l = g2l(g, w0, W)
26      f_Rabi = 2 * l /eta
27      delta_r = W - w0
28      delta_b = w0 + W
29
30      init = tensor(basis(2, 1), basis(N, 0))
31      tlist = np.linspace(0, 0.02, 1000)
32      laser1 = Laser(omegaI - nu + delta_r, eta, f_Rabi)
33      laser2 = Laser(omegaI + nu + delta_b, eta, f_Rabi)
34      H = H_RWA(N, omegaI, nu, [laser1, laser2])
35
36      result = mesolve(H, init, tlist, [sqrt(2 * kappa) * a], [a.dag() * a],
37                      options=Options(nsteps=6000))
38      return result
39
40
41  # Run on server (~2h for each ratio, very laborous)
42  for ratio in ratiolist:
```

```python
43      W = ratio * w0
44      print('ratio=', ratio)
45      result = parallel_map(func, xlist[ratio], progress_bar=True)
46      qsave(result, f'ratio_{ratio}')  # save result for each ratio for safety
47      ylist[ratio] = [re.expect[0][-1] for re in result]
48  qsave(ylist, 'ion_ffs_result')  # save altogether result
49
50
51  # Run the following line if loading from a pickled file.
52  # ylist = qload('./ion_ffs_result')
53
54
55  # QRM FFS function as comparison
56  N = 100  # very fast for QRM Hamiltonian, ~10s for each ratio
57  a = destroy_a(N)
58  etalist = [30, 40, 50, 100]
59  xlist = {etalist[i]:np.logspace(-4.5 + 0.13 * i, -2 + 0.13 * i, 12) for i in range(4)}
60  ylist2 = {30:[], 40:[], 50:[], 100:[]}
61  for eta in etalist:
62      W = eta * w0
63      for x in xlist[eta]:
64          g = gc - (x / eta) ** (1 / 2)
65          l = g2l(g, w0, W)
66          steady = steadystate(H_QRM(w0, W, l, N), [np.sqrt(2 * kappa) * a])
67          aa = expect(a.dag() * a, steady)
68          y = np.abs(g - gc) ** 1 * aa
69          ylist2[eta].append(y)
70
71
72  # Plot
73  from mpl_toolkits.axes_grid1.inset_locator import inset_axes
74  symblist = {30:'o', 40:'*', 50:'^', 100:'X'}
75
76  # main axis
77  plt.figure(figsize=(5, 3))
78  fig, ax = plt.subplots(figsize=(5, 3), constrained_layout=True)
79  for ratio in ratiolist:
80      ax.plot(xlist[ratio], ylist[ratio], f'{symblist[ratio]}', label=ratio, markersize=5)
81  ax.set_xlabel(r'$\left(\Omega/\omega_0\right)\left|g-g_c\right|^2$', fontsize=11)
82  ax.set_ylabel(r'$\left|g-g_c\right|^1\langle a^\dagger a\rangle$', fontsize=11)
83  ax.set_xscale('log')
84  ax.set_yscale('log')
85  ax.legend(title=r'$\Omega / \omega_0$')
86
87  # inset
88  inset_ax = inset_axes(ax, 1.6, 0.96, bbox_to_anchor=(0.96, 0.54), bbox_transform=ax.transAxes)
89  for ratio in ratiolist:
90      inset_ax.plot(xlist[ratio], ylist2[ratio]-ylist[ratio], f'{symblist[ratio]}', markersize=4)
91  inset_ax.set_xscale('log')
92  inset_ax.set_yscale('log')
93  inset_ax.text(0.26 * 10**(-4), 2.5 * 10**(-4), 'deviation', rotation=90, fontsize=9)
94
95  plt.savefig('./plots/ion_ffs.pdf')
```

Acknowledgements

Throughout the writing of this thesis, I have received a great deal of support and assistance. I am deeply grateful to my supervisor, Professor Kim Kihwan. His expert advice and perspicacious feedback made it possible for me to grow from a dabbler to a trained student in experimental physics. Although I am going to study theoretical physics as a doctoral student, I will cherish the experience in his group. Prof. Kim is patient and never pushy. He offers me his encouragement and allows me to take my time whenever I was stuck in hesitation or in a dilemma.

I would like to express my appreciation to brilliant colleagues in our group. The senior doctoral students, Qiao Mu, Dr Wang Pengfei, and Luan Chunyang provide me with careful guidance in both theoretical study and experimental operation. Members belonging to other projects, including Cai Zhengyang, Chen Wentao, Zhang Jialiang, and Yu Jingfan, are also very cordial to me. I would like to thank the smart theorist Liu Zidu from our neighboring group, for the fruitful conversations I had with him. These people have made my research career here in Tsinghua University relaxing and cheerful. Particularly, I will not forget their generosity in lending me their meal cards.

I would like to extend my sincere thanks to professors from the School of Physics, Peking University. When I just entered the School of Physics, I was not confident enough and was once deeply discouraged by the difficulty of thermodynamics. At that time Prof. Mu Liangzhu gave me very powerful encouragement that changed my understanding of myself. Prof. Yang Lilin addressed impressive lectures on programming basics. Prof. Wang Jianwei offered me a precious opportunity to participate in a project to work with integrated quantum photonics. Many teachers have impressed me and sorry to not be able to name them all.

I will not forget the support and encouragement I have received from my friends during the years. Young physicists here in the School of Physics are very talented and helped me a lot in my academic work and school life. I enjoy every meeting with friends from Chengdu: we share our nostalgia for Sichuan cuisine and our suffering nowadays, which is really healing. I enjoy every reunion with my childhood friend; we are still linked to each other closely notwithstanding the distance between us.

Of course I am also grateful to my family members, who have left me enough freedom to make choices for my future. Finally, I would like to acknowledge my girlfriend and good

companion Wang Xiao. Able to stay together or not, I firmly believe that we are extraordinary people and will have a bright future.

<div align="center">

FORSAN ET HAEC ŌLIM MEMINISSE IVVĀBIT.

(*Virgilius*)

</div>